Design of an Aerial Manipulator with Active Moment Compensation

Manas Reddy Ramidi



Delft University of Technology

TU Delft

Design of an Aerial Manipulator with Active Moment Compensation

by

Manas Reddy Ramidi

to obtain the degree of Master of Science
at the Delft University of Technology,
to be defended publicly on 19 August, 2026 at 01:00 PM.

Student number:	6191258	
Project duration:	January, 2026 – August, 2026	
Thesis committee:	Prof.dr. J. Alonso-Mora,	TU Delft, Chair
	Dr. S. Sun,	TU Delft, Supervisor
	Prof.dr.ir. M. Wisse,	TU Delft
	Ir. T. Minten,	TU Eindhoven / SpectX, Supervisor

Cover:	A drone flying through a sunset sky by Hyory Liu under Unsplash License
Style:	TU Delft Report Style, with modifications by Daan Zwaneveld

An electronic version of this thesis is available at `http://repository.tudelft.nl/`.

TU Delft

Acknowledgments

This thesis marks the end of a genuinely rewarding two years of master's study at TU Delft. I want to thank everyone who supported me along the way, directly or indirectly.

I am deeply grateful to SpectX for this practical opportunity, to Mani Kamalzadeh, Akhilesh Goveas, and the rest of the team for being such an important part of this journey, and for helping me grow from an intern into an engineer. Thanks to Luis and Ali for helping out with the electronics and hardware tasks. Special thanks to Tom Minten, my project collaborator, for going through this journey with me, always being ready to lend a hand and insights to navigate this complex project.

I would like to thank Professor Javier for accepting this thesis and for the positive energy he brought to every meeting, despite our limited interactions. Also, special thanks to Dr. Sun, my daily supervisor at the university, who stayed closely involved from my internship onwards. Thank you for patiently answering my endless questions, providing invaluable insights whenever I needed them, and being especially supportive during the early, uncertain stages of this project.

I would also like to thank the Writing Center for organizing the Thesis Boost Days, and the coaches, Mirte and Robin, for bringing their editorial expertise and human insight to improve this report, and also for creating a warm environment that made the tedious writing phase more manageable.

On a personal note, I am grateful to all my friends I met through the MSc Robotics program for making the academic environment so enjoyable. A special thanks to my classmates Prajwal and Pradyun for staying close during this journey, and to my housemates and gang at Polakweg - Rikin, Juvvi, Muthu, Abhishek, Supriya, Srishti, and Akshita - for keeping me sane outside of university life and for all the memorable moments and rants we shared over the past 2 years.

I am equally thankful to Ieshir, Devika, and all my friends from India for taking the time to stay in touch or share memes despite the distance and our increasingly busy lives. Above all, I cannot thank my family enough for always doing everything they could to make my life abroad easier and more comfortable. Their unwavering support made this journey possible.

I want to sincerely acknowledge the efforts of the open-source community for developing remarkable software such as ROS and PX4, which are integral not only to this thesis but to the broader field of robotics. I also acknowledge the use of AI tools for help with understanding complex concepts, code, and language refinement.

This has, without a doubt, been one of the most transformative chapters of my life. I am eager to apply what I've learned at Delft to solve the world's engineering challenges and keep persevering.

Manas Reddy Ramidi
Delft, August 2026

Abstract

Unmanned Aerial Manipulators (UAMs) have revolutionized industrial infrastructure inspection. But when a drone deploys an extended manipulator arm to carry dense Non-Destructive Testing (NDT) sensors, the payload severely shifts the system's Center of Gravity (CoG). This forward shift generates static pitch torques that can quickly overwhelm and saturate standard flight controllers.

To resolve this, this thesis presents the design, digital simulation, and experimental flight validation of a novel aerial manipulator. The architecture features a 1-Degree-of-Freedom (1-DOF) parallel linkage equipped with auxiliary tip motors. This system utilizes an Active Moment Compensation (AMC) strategy, in which the tip rotors generate dedicated vertical lift to continuously counteract the payload's gravitational torque, fundamentally decoupling the manipulator's reach from the primary quadrotor's stabilization limits. Before physical deployment, the control logic was validated in a high-fidelity Software-in-the-Loop (SITL) digital twin using ROS 2 and Gazebo Harmonic. Crucially, the PX4 Control Allocator was mathematically extended from a standard 4-rotor matrix to a custom 6-rotor geometry, enabling the autopilot to natively map thrust across the system.

Extensive parametric flight testing proved the core kinematic hypothesis: because the parallel linkage forces the tip-rotors to remain perfectly horizontal, the required compensation thrust is a mathematical constant, completely independent of the arm's pitch angle. Experimental data confirmed that the AMC architecture neutralizes extreme CoG shifts while preserving the dynamic thrust headroom required for stable flight. Additionally, vibration and telemetry analyses demonstrated that elevating the mechanism isolates it from the primary rotor downwash, reducing structural resonance and altering attitude control performance. By successfully de-risking this active-thrust architecture, this research provides a rigorously verified, scalable framework for deploying heavy industrial sensors at extended standoffs.

Contents

Acknowledgments i

Abstract ii

Nomenclature v

1 Introduction 1
- 1.1 Motivation . . . 1
- 1.2 Objectives and Research Questions . . . 2
- 1.3 Report Outline . . . 2

2 Literature Review 4
- 2.1 Operational Paradigms in Aerial Manipulation . . . 4
- 2.2 The Dynamic Coupling and CoM Shifting Problem . . . 4
- 2.3 Hardware Evolution: Rigid Arms to Distributed Actuation . . . 5
- 2.4 Non-Contact Inspection Regime . . . 6
- 2.5 Synthesis of Research Gaps . . . 7

3 Modeling 8
- 3.1 Static Torque & Kinematic Decoupling . . . 8
- 3.2 Dynamic & Theoretical Modeling . . . 9
- 3.3 Parametric State definition for Baseline Validation . . . 10
- 3.4 Inertial Scaling to Full-System Dynamics . . . 10

4 Mechanical Design, Fabrication and Avionics 11
- 4.1 Additive Manufacturing and Material Selection . . . 11
- 4.2 Structure Assembly . . . 12
- 4.3 Payload Distribution . . . 13
- 4.4 Actuation and Power Distribution . . . 13
- 4.5 Electronic Routing and Interconnects . . . 15
- 4.6 Telemetry and Control Bypass Architecture . . . 16

5 Control Architecture 18
- 5.1 Cascade Control Architecture . . . 18
- 5.2 Theoretical Formulation of the Control Allocator . . . 18
- 5.3 Dual-Mode Control Strategy for Parametric Validation . . . 19

6 Simulation 21
- 6.1 PX4-ROS-Gazebo Architecture . . . 21
- 6.2 Rotor Integration and Mathematical Calibration . . . 23
- 6.3 PX4 Control Allocator Extension . . . 24
- 6.4 Dual-Mode Control Architecture for Simulation . . . 25
- 6.5 Validation . . . 25

7 Experimental Validation (Flight Tests) 27
- 7.1 Phase 1: System Integration and Open-Loop Baseline ($\theta = 0°$) . . . 27
- 7.2 Phase 2: Closed-Loop Autonomous Evaluation ($\theta = 0°$) . . . 28
  - 7.2.1 System Upgrade and Parameter Resolution . . . 29
  - 7.2.2 The Loaded Anomaly: Unmodeled CoG Translation . . . 30
- 7.3 Phase 3: Parametric Kinematic Evaluation . . . 32
  - 7.3.1 Theoretical Validation: The $\cos\theta$ Decoupling . . . 33
  - 7.3.2 Elevated State Evaluation ($\theta = 15°$) . . . 33
  - 7.3.3 Depressed State Evaluation ($\theta = -15°$) . . . 36

7.3.4 Maximum Elevation State Evaluation ($\theta = 30^\circ$) 36
7.4 Discussion and Implications for Dynamic Control 36

8 Conclusion **40**

References **42**

A SITL Software Configuration Architecture **45**
A.1 ROS 2 Workspace and Package Structure 45
A.2 PX4 Airframe Geometry and ESC Mapping 45
A.3 Launch Configuration and Dual-Mode YAML 46
A.4 Verification 47

B Pictures during the process **48**

Nomenclature

Abbreviations

Abbreviation	Definition
AMC	Active Moment Compensation
AWG	American Wire Gauge
CA	Control Allocator
CAD	Computer-Aided Design
CCW	Counter-Clockwise
CF	Carbon Fiber
CoG	Center of Gravity
CoM	Center of Mass
CW	Clockwise
DOF	Degree of Freedom
ESC	Electronic Speed Controller
FDM	Fused Deposition Modeling
FFT	Fast Fourier Transform
FMU	Flight Management Unit
IMU	Inertial Measurement Unit
NDT	Non-Destructive Testing
PETG	Polyethylene Terephthalate Glycol
PID	Proportional-Integral-Derivative
PLA-CF	Polylactic Acid reinforced with Carbon Fiber
PSD	Power Spectral Density
PWM	Pulse Width Modulation
RC	Radio Control
RCOUT	Actuator Output (PX4 Telemetry)
RMSE	Root Mean Square Error
ROS	Robot Operating System
RPM	Revolutions Per Minute
SBUS	Serial Bus
SITL	Software-in-the-Loop
UAM	Unmanned Aerial Manipulator
UAV	Unmanned Aerial Vehicle

Symbols

Symbol	Definition	Unit
C_d	Rotor drag coefficient	[N·m·s^2/rad^2]
D	Fastener hole diameter	[mm]
e	Fastener edge distance	[mm]
e/D	Edge Distance Ratio	[–]
F	Thrust force	[N]
F_{max}	Maximum theoretical combined thrust capacity	[N]
F_{thrust}	Combined active compensation thrust	[N]
g	Gravitational acceleration	[m/s^2]
H_m	Dynamic headroom margin	[%]
I	Electrical current	[A]
I_{xx}, I_{yy}, I_{zz}	Principal moments of inertia	[kg·m^2]
I_{boom}	Moment of inertia of the scaled boom	[kg·m^2]
k_m	Motor moment coefficient	[m]
k_T	Motor thrust coefficient	[N·s^2/rad^2]
L_{boom}	Primary boom projection length	[m]
l_x, l_y	Longitudinal and lateral moment arms of main rotors	[m]
M_{total}	Total mechanism payload mass	[kg]
m_{base}	Mass of the unloaded X500 chassis	[kg]
m_{load}	Mass of the attached external payload	[kg]
m_{src}, m_{dtr}	Discrete mass of the source and detector payloads	[kg]
P_{mech}	Mechanical shaft power	[W]
R	Electrical resistance	[Ω]
T_{front}, T_{rear}	Combined lift of the front and rear main rotor pairs	[N]
T_{main}	Total lift generated by the primary main rotors	[N]
V	Electrical voltage	[V]
x_{tip}, z_{tip}	Position of the tip link in local coordinate frame	[m]
Δx_{cg}	Forward longitudinal translation of the physical Center of Gravity	[m]
η	Electrical/Mechanical efficiency factor	[–]
θ	Kinematic pitch angle of the parallel manipulator boom	[°]
$\ddot{\theta}$	Angular acceleration of the manipulator boom	[rad/s^2]
ρ	Density	[kg/m^3]
τ	Reaction torque / physical pitch torque	[N·m]
τ_g	Static gravitational torque	[N·m]
τ_{root}	Sum of static moments around the root pivot	[N·m]
τ_{thrust}	Torque generated by the active tip-actuators	[N·m]
τ_{up}, τ_{down}	Spin-up and spin-down motor time constants	[s]
$\tau_{y,phys}$	Actual physical pitch torque exerted on the airframe	[N·m]
$\tau_{y,soft}$	Commanded software pitch torque setpoint	[N·m]
ω	Angular velocity of the rotor	[rad/s]
$\dot{\omega}$	Angular acceleration of the rotor	[rad/s^2]

1

Introduction

The integration of robotic manipulators with Unmanned Aerial Vehicles (UAVs) has led to the emergence of Unmanned Aerial Manipulators (UAMs), allowing for active operations in hazardous or inaccessible environments. Aging civil and energy infrastructure, such as high-voltage transmission networks, offshore wind turbines, and nuclear facilities, requires continuous monitoring to prevent catastrophic failures that incur massive economic and environmental costs.

Traditionally, inspecting these structures relies on rope-access technicians, heavy scaffolding, or cranes, which are expensive and pose severe human safety risks. While standard UAVs have revolutionized passive visual inspection, they cannot deploy contact-based or proximity-restricted Non-Destructive Testing (NDT) sensors. Bridging this gap through UAMs promises a paradigm shift in infrastructure maintenance: drastically reducing operational downtime, eliminating human risk in hazardous zones, and extending the operational lifespan of critical assets.

1.1. Motivation

Standard NDT with X-Ray relies on two distinct modules: a source and a detector. Currently, the common aerial approach involves flying these components on two separate drones [20, 16], a method that requires complex mid-air alignment and introduces redundancy, as seen in Figure 1.1. Consolidating both sensors onto a single drone using a long manipulator arm offers a much cleaner solution. However, the development of these long-reach aerial manipulators is bottlenecked by the ”Long-Reach Weight Paradox”. Extending a dense NDT payload at the end of a rigid kinematic chain drastically shifts the system’s global Center of Gravity (CoG) forward, generating significant static pitch torques at the root joint [10].

Conventional solutions fail to address the root physics of this problem: heavy proximal joint servos rapidly deplete battery endurance [13]; conventional passive sliding counterweights add complexity of mechanism and dead mass [2, 26, 7]; and relying solely on the UAV’s default control method to reject torque rapidly saturates the main lift rotors, leading to a catastrophic loss of control authority [15]. A novel hardware and control architecture is required to decouple the manipulator’s reach from the UAV’s torque limits.

This problem is part of the public project Shocking Precision: X-Ray Tech and Autonomous Drones Power the Future of Grid Inspection, undertaken by a consortium of SpectX, TU/e, Avular, and TenneT as part of the EFRO OP Zuid Subsidy program [6, 31]. The basic requirement is to create a drone-based mechanism to carry the source and detector sensors, each weighing about 2.5 kg. The initial requirement was set as a 2.5 m-long mechanism to carry this payload under the required inspection conditions. To solve this problem, we decided to develop a small-scale prototype, validate ideas, and carry over the insights to full-scale implementation.

To tackle this problem with a new approach, this thesis proposes the design, modeling, and rigorous parametric validation of a novel long-reach aerial manipulator equipped with active distributed thrust.

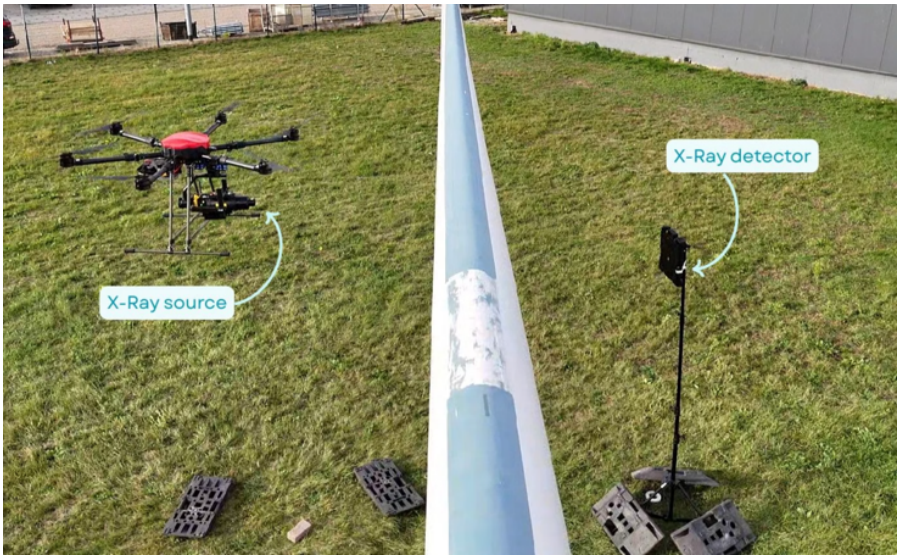


Figure 1.1: X-ray sensors with UAV flight test carried out by SpectX

Rather than relying on passive counterweights, the architecture utilizes a 500 mm parallel four-bar linkage equipped with dual, counter-rotating auxiliary motors at the distal crossbar. By generating a local vertical lift vector, these tip motors cooperatively offload root joint torque to achieve Active Moment Compensation (AMC), thereby creating a dynamically compensated floating cantilever for a stable, non-contact NDT deployment.

1.2. Objectives and Research Questions

The primary objective of this research is to solve the ”Long-Reach Weight Paradox” inherent in aerial manipulation. Traditional UAVs designed for NDT inspections struggle to carry extended manipulator arms without experiencing severe center-of-gravity (CoG) shifts that compromise flight stability. To overcome this, the thesis proposes an Active Moment Compensation (AMC) architecture that introduces active rotor thrust at the end effector.

Using a Holybro X500 drone, this project aims to validate the kinematic stability and structural integrity of this novel mechanism and establish a baseline control framework that can later be scaled up for industrial implementation. To achieve this, the thesis addresses the following core research questions:

- **Theoretical Model (Kinematics):** How can the geometric advantage of a parallel four-bar linkage (Figure 3.1) and thrust compensation concepts be leveraged and modeled to simplify flight control for payload?
- **Mechanism Prototype (Fabrication):** What are the optimizations and design decisions for the components to ensure the structural rigidity of the parallel linkage against the torsional roll loads of the tip-rotors?
- **Digital Validation (Simulation):** Before engaging in physical flight trials, how can a custom 6-motor control allocation strategy be effectively integrated and validated within a high-fidelity PX4 [21] Software-in-the-Loop (SITL) digital twin?
- **Real-World Dynamics (Experimental Validation):** When subjected to physical flight testing across a discrete parametric envelope ($\theta = \{0°, \pm 15°, 30°\}$), how do unmodeled physical forces, such as aerodynamic cross-axis coupling and structural stress, affect the drone’s stability and the limits of the standard flight controller?

1.3. Report Outline

This report is structured as follows: Chapter 2 reviews the current state of the literature on aerial manipulation and identifies gaps to address. Chapter 3 formulates the mathematical kinematics and AMC

decoupling theory. The subsequent Chapter 4 delves into how the modeling is realized through mechanical fabrication and the avionics architecture. Chapter 5 details the working of the control architecture for the mechanism. Chapter 6 presents the creation and testing of the SITL simulation for the architecture. Chapter 7 analyzes empirical flight-test data across the parametric envelope. Finally, Chapter 8 concludes the research and outlines the trajectory for full-scale dynamic integration. The Appendix expands on the technical details and parameters for Simulation work in Chapter A. It concludes with Chapter B, which includes additional pictures from the thesis process and a detailed overview through the Thesis Gantt Chart B.3.

2

Literature Review

This chapter presents an assessment of current state-of-the-art methods and design ideas obtained through a systematic literature search of the IEEE Xplore, Scopus, and Google Scholar databases. The search strategy employed Boolean combinations of the following primary keywords: (”Unmanned Aerial Manipulator” OR ”Aerial Manipulation”) AND (”Center of Mass” OR ”Dynamic Coupling” OR ”Weight Compensation” OR ”Distributed Thrust” OR ”Non-Destructive Testing”). The inclusion criteria focused on peer-reviewed journal articles and top-tier conference proceedings published, prioritizing empirical studies that addressed payload limitations, CoG shifting, and novel actuation architectures. To counteract CoG displacement, the literature reports several mechanical interventions, ranging from heavy proximal servos and passive sliding counterweights to overactuated multirotors (Figure 2.1). The literature specifically related to distributed thrust and mechanisms with additional motors was found to be limited. However, by following citation chains and using literature discovery tools such as Research Rabbit, relevant studies were identified and systematically aggregated to provide the most comprehensive review possible.

2.1. Operational Paradigms in Aerial Manipulation

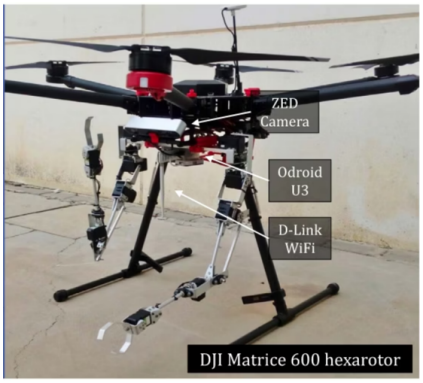
Within the literature, UAM applications are broadly bifurcated into two operational paradigms: contact-based physical interaction and non-contact spatial positioning. Contact-based manipulation requires the end-effector to exert sustained forces against the environment for tasks such as tactile inspection or grasping. In these applications, the primary engineering challenge is managing the complex reaction wrenches transmitted from the environment to the floating aerial base.

Conversely, non-contact manipulation involves no physical interaction with the target infrastructure. Instead, the manipulator is used to spatially position sensitive diagnostic payloads at precise standoff distances. While non-contact operations bypass environmental reaction wrenches, they pose a paradoxical design challenge: achieving sufficient reach to safely penetrate occluded zones while maintaining the stringent spatial stability required by non-contact sensors. The extension of long, rigid kinematic chains induces massive Center of Mass (CoM) shifts and structural vibrations, rapidly saturating the UAV’s flight controller.

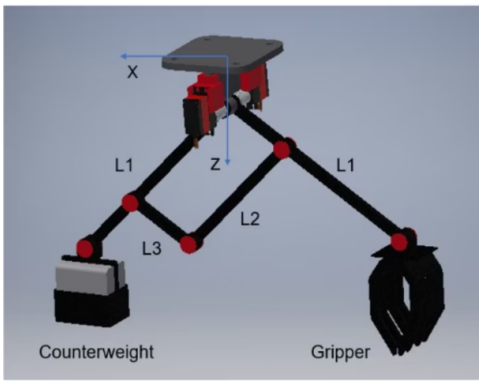
2.2. The Dynamic Coupling and CoM Shifting Problem

Unlike ground-based mobile manipulators, UAMs are highly susceptible to dynamic coupling between the aerial platform and the extending mechanism. The standard Equations of Motion (EOM) explicitly capture these coupling effects in the system inertia matrix, which contains off-diagonal terms representing inertial crosstalk between the arm and the drone [24]. As the manipulator extends, the system’s CoM moves away from the UAV’s geometric center, generating undesirable static torques that directly degrade the vehicle’s position, attitude, and stability [10].

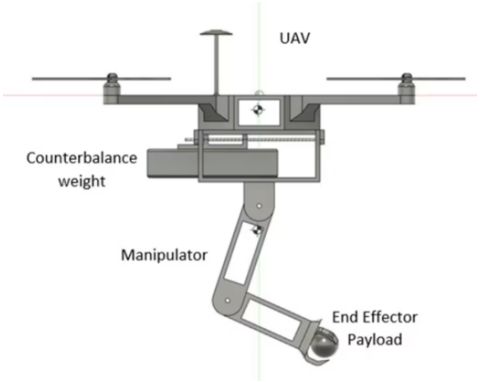
To stabilize the platform, the literature details two primary architectural paradigms:



(a) Servos [32]



(b) Counterweight [2]



(c) Sliding battery [3]



(d) Over-actuation [33]

Figure 2.1: Different aerial manipulator mechanisms discussed across the literature

Decoupled Control: This framework treats the UAV and the manipulator as independent systems, modeling reaction torques merely as external disturbances to be rejected by the UAV's flight controller. While robust enough for quasi-static inspection tasks, decoupled schemes exhibit deteriorating tracking fidelity during high-dynamic maneuvers [15]. Because the controller treats CoM shifts as unmodeled disturbances, it is forced to use a reactive stabilization strategy, which often leads to oscillation or motor saturation under heavy payloads.

Coupled Control: Centralized architectures, such as Model Predictive Control (MPC), treat the UAM as a holistic multibody system derived via Euler-Lagrange or Newton-Euler formulations [32], with nonlinear techniques such as feedback linearization theoretically enabling simultaneous, high-fidelity control of both the vehicle and the end-effector [25]. However, this approach is computationally intensive and relies heavily on precise model identification; obtaining accurate parameters is often complicated by unmodeled aerodynamic uncertainties, which can degrade stability if the model diverges from reality [10].

To counteract CoM displacement without full dynamic modeling, algorithmic interventions such as Variable Parameter Integral Backstepping (VPIB) [14] or active counter-balancing [2, 3] have been proposed to adjust the UAV's attitude or redistribute mass preemptively. However, relying solely on algorithms or sliding batteries does not address the root mechanical limits of proximal joint torque under extended lever arms.

2.3. Hardware Evolution: Rigid Arms to Distributed Actuation

The need to balance manipulation dexterity with flight endurance has been a central challenge in the development of aerial manipulators. Historically, the field relied on a "rigid integration" paradigm, wherein standard industrial arms were mounted directly onto aerial platforms. Although offering kinematic stiffness, the substantial mass drastically curtailed flight endurance, and the large moments of inertia ne-

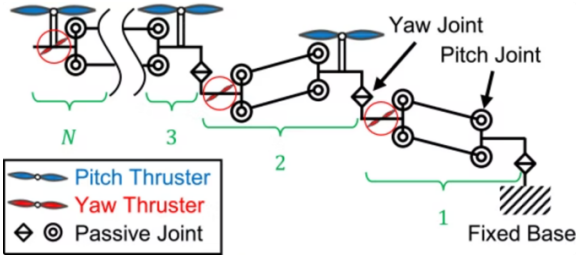
cessitated complex control compensation [13]. In response, contemporary literature has pivoted toward ”inertia-optimized” architectures:

Remote Actuation: By relocating servo actuators to the aerial base and transmitting motion through cable or belt networks, researchers have significantly reduced the rotational moment of inertia of the distal links [3, 19].

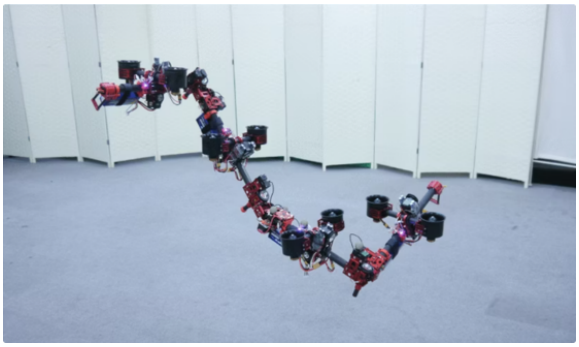
Parallel Linkages: Structural innovations, such as pantograph-inspired mechanisms, minimize structural weight while inherently preserving the UAV's CoG alignment.

However, as noted by Yang et al. [35], conventional proximal actuation suffers from load accumulation, making long-reaching aerial manipulation unfeasible with standard base motors due to exponential torque scaling.

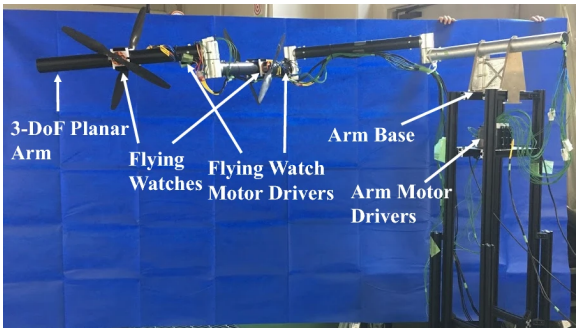
To address this fundamental scaling limitation, distributed thruster actuation has emerged as a transformative architecture. By installing propellers directly on the manipulator links to generate local lift, the manipulator is freed from gravity's constraints [12]. Modular thrust augmentation devices [27] and fully articulated aerial skeletons [34, 35, 37] demonstrate that compensating for the gravitational moment of each link individually effectively decouples the link length from the base joint's torque limits, allowing remarkable reach-to-weight ratios. Some of the relevant mechanisms are shown in Figure 2.2.



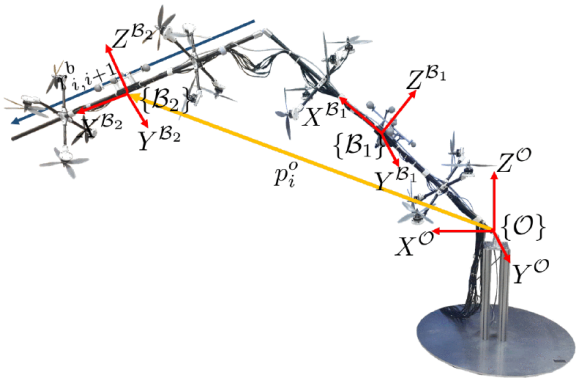
(a) Hiryu-II [34]



(b) DRAGON [37]



(c) Flying watch [27]



(d) LASDRA [35]

Figure 2.2: Distributed thruster actuation mechanisms discussed across the literature

2.4. Non-Contact Inspection Regime

In infrastructure monitoring, avoiding contact is a strict requirement, particularly when working around energized or complex assets. As a result, aerial inspection systems must maintain high spatial stability. Adapting terrestrial NDT techniques to UAV platforms introduce several challenges. High-fidelity visual inspection and thermography require super-long-reach articulated manipulators to project cameras into hazardous zones without risking the UAV's base [8]. Other methods, such as Electromagnetic Acoustic Testing (EMAT) and X-ray imaging, place even stricter demands on positioning, requiring air gaps as small as 3 mm or precise spatiotemporal synchronization [36].

The transition to these dense NDT payloads significantly alters the system's inertia tensor and increases battery consumption. Additionally, the flexibility of extended, lightweight manipulator links amplifies high-frequency motor vibrations, causing severe sensor blur [20]. Maintaining the required standoff distance is further complicated by ground-effect turbulence and other dynamic disturbances, especially since the system cannot rely on physical contact for stabilization.

2.5. Synthesis of Research Gaps

The transition from passive observation to active NDT positioning requires projecting heavy payloads deep into occluded zones. The current literature fails to resolve this due to three critical gaps:

1. *The Long-Reach Weight Paradox:* Standard rigid-arm architectures impose a weight penalty that rapidly saturates the base actuators. While mechanical balancing mitigates CoM shift, it does not solve the exponential torque required at the proximal joint.
2. *Inadequacy of Passive Hardware:* Existing solutions rely on passive counterweights (adding dead mass) or force the flight controller to reject massive inertial disturbances. There is a distinct lack of hybrid architectures optimized for high-precision spatial regulation.
3. *The Non-Contact Disturbance Regime:* The vast majority of the literature focuses on regulating wrenches with physical contact. The field lacks methods that address the structural elasticity and stabilization of a long, floating cantilever in the presence of rotor-induced turbulence.

In response to these identified gaps, this research proposes the design and empirical validation of an active-thrust parallel manipulator. By utilizing distributed thrust to offload joint torque and regulate the system's global CoG, this architecture provides the dynamic headroom necessary for stable, non-contact NDT deployment. The mathematical formulation proving this kinematic decoupling is established in Chapter 3.

3

Modeling

This chapter details the force-torque calculations used to model the mechanism. The foundation of this aerial manipulator mechanism is a 1-Degree-of-Freedom (1-DOF) parallel four-bar linkage (Figure 3.1). Unlike a rigid cantilever beam, the parallel linkage guarantees that the tip link and the attached crossbar with tip motors remain completely horizontal relative to the drone chassis, regardless of the boom's pitch angle (θ). For the scaled-down prototype, the linkage is defined by a primary boom length of $L_{boom} = 500$ mm. The system's state can be defined by the root joint angle alone. The position of the tip link in the drone's local coordinate frame (x_{tip}, z_{tip}) is derived as:

$$x_{tip} = L_{boom}\cos(\theta), z_{tip} = -L_{boom}\sin(\theta) \tag{3.1}$$

This parallel-link-induced geometric constraint simplifies the control architecture, as the control for tip motors only needs to govern the rotational pitch axis, while the thrust vector of the tip motors remains vertical.

3.1. Static Torque & Kinematic Decoupling

The primary disturbance introduced by an aerial manipulator is the massive pitching moment acting on the drone's center of mass. To prevent the primary flight controller from saturating its forward lift motors, this architecture employs active tip rotors to achieve AMC at the root joint. Because the mechanism utilizes a parallel four-bar linkage, the tip link remains geometrically parallel to the local drone inertial frame $\mathcal{F}_L$. Being fixed to the tip link, the thrust vector of the dual tip-motors (F_{thrust}) remains vertical irrespective of the boom angle θ. A free body diagram of the mechanism is shown in Figure 3.1.

The static torque generated by gravity (τ_g) is a function of the horizontal projection of the moment arms:

$$\tau_g(\theta) = g\cos\theta\,(m_{src}d_{src} + m_{dtr}d_{dtr} + m_{boom}d_{cm\_boom}) \tag{3.2}$$

The counter-torque generated by the active tip rotors (τ_t) relies on the same horizontal projection:

$$\tau_t(\theta) = F_{thrust}\cdot(L_{boom}\cos\theta) \tag{3.3}$$

To establish the AMC, the sum of moments around the root pivot ($\sum\tau_{root}$) must be equal to zero. The total payload mass ($M_{total} = 500$ g) is distributed between two discrete nodes to minimize static torque: a source node (m_{src}) and a detector node (m_{dtr}). The equilibrium equation is formulated as:

$$\sum\tau_{root} = F_{thrust}\cdot(L_{boom}\cos\theta) - (g\cos\theta\,(m_{src}d_{src} + m_{dtr}d_{dtr} + m_{boom}d_{cm\_boom})) = 0 \tag{3.4}$$

Where F_{thrust} is the combined upward aerodynamic force generated by the dual tip-motors. m_{src} and m_{dtr} represent the 250 g payloads. d_{src} and d_{dtr} are their respective moment arms, 100 mm and 350 mm. τ_{boom} is the inherent torque generated by the masses of the 16 mm diameter carbon fiber

tube, bracket, crossbar, and motors. Solving for the required active compensation thrust yields the following:

$$F_{thrust} = \frac{(m_{src} \cdot g \cdot d_{src}) + (m_{dtr} \cdot g \cdot d_{dtr}) + (m_{boom} \cdot g \cdot d_{cm\_boom})}{L_{boom}} \tag{3.5}$$

This mathematical cancellation of $\cos\theta$ is the core architectural advantage of combining thrust compensation with a parallel linkage. The required AMC thrust is proven as a kinematic constant, independent of the pitch angle of the mechanism θ. Hence, the payload compensation logic is decoupled from the arm's trajectory, eliminating the need for complex feed-forward calculations within the flight controller. Substituting and solving the Equation 3.5 yields the required $F_{thrust} \approx$ *4.02 N or 205 g* for a single motor pull value.

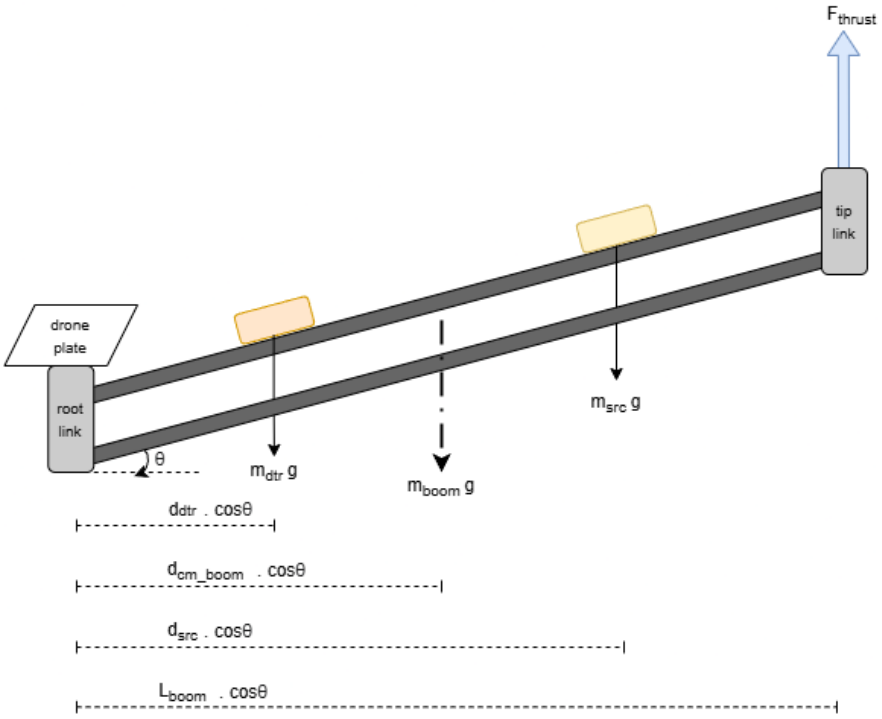


Figure 3.1: Simplified diagram of the forces on the mechanism

3.2. Dynamic & Theoretical Modeling

While static equilibrium prevents drone motor saturation during hover, the active thrust system must maintain sufficient control authority, or headroom, to reject dynamic disturbances, such as wind gusts or aggressive translational braking [22]. The system utilizes dual brushless DC motors mounted on a 150 mm transverse crossbar in a counter-rotating, props-out configuration, with a maximum theoretical combined thrust capacity of F_{max}. Comparable counter-rotating multirotor configurations are conventionally designed such that hover equilibrium falls within a 50-60% throttle band, reserving the remaining capacity for control authority beyond static equilibrium [18]. The dynamic headroom margin (H_m) can be expressed as a percentage of unused thrust capacity at static equilibrium:

$$H_m = \left(1 - \frac{F_{thrust}}{F_{max}}\right) \cdot 100 \tag{3.6}$$

Greater headroom is desirable, as it provides greater thrust capacity to maintain stability under disturbances. If the value of F_{thrust} approaches that of F_{max}, the tip rotors saturate, the AMC assumption fails, and the resulting uncompensated torque would be transferred to the drone chassis.

3.3. Parametric State definition for Baseline Validation

While the theoretical torque remains constant, altering the fixed boom angle θ introduces secondary physical disturbances that must be empirically verified. The system is evaluated across a discrete set of parametric angles: $\theta = \{0°, 15°, -15°, 30°\}$. As θ increases, the horizontal displacement of the payload mass ($x_p = L_{boom} \cos\theta$) decreases, causing the global Center of Gravity (CoG) of the vehicle to shift up and inward toward the root joint. Moreover, the elevation of the tip rotors ($z_p = L_{boom} \sin\theta$) alters their position relative to the main rotors. The parametric flight tests are designed to verify that the PX4 attitude controller can reject dynamic CoG shifts and aerodynamic disturbances, while the AMC tip rotors handle the static load.

3.4. Inertial Scaling to Full-System Dynamics

To safely validate the active Active Moment Compensation (AMC) architecture, the physical prototype was constrained to a 1:5 linear scale and a 1:10 mass scale representation of the target heavy sensors.

Rather than applying a single isotropic geometric expansion (the square-cube law), the scaling factors were decoupled to accurately reflect the real-world constraints of aerial inspection. This follows established distorted-similitude practices, treating mass, length, and inertia as independently derived quantities [4].

For length, the full-size platform requires a 2.5 m standoff to ensure proper clearance during inspections. By designing a 0.5 m prototype boom, a linear scale factor of $k_l = 1 : 5$ is established. For mass, the scaling was driven by the target NDT X-Ray suite's actual weight (approximately 5.0 kg). This is represented with a 500 g distributed dummy load on the prototype, yielding a mass scale factor of $k_m = 1 : 10$.

This decoupled scaling deliberately isolates the most critical dynamic threat to long-reach aerial manipulation: the non-linear amplification of rotational inertia. Approximating the payload as a point mass, the prototype's moment of inertia (I_{proto}) and the target moment of inertia (I_{target}) relative to the root joint scale according to:

$$I_{target} = k_m \cdot (k_l)^2 \cdot I_{proto}$$

Substituting the established mass and length scaling factors yields:

$$I_{target} = 10 \cdot (5)^2 \cdot I_{proto} = 250 \cdot I_{proto} \tag{3.7}$$

This calculation highlights exactly why the proposed active-thrust architecture is necessary. While the absolute payload mass increases by an order of magnitude (10x), the rotational inertia increases by a factor of 250. Scaling a traditional, passive, rigid arm to these dimensions would generate a dynamic reaction torque that would far exceed the saturation limits of any commercial flight controller. Hence, validating the AMC logic on this physical prototype will demonstrate the control methodology required to arrest the massive $250 \times I_{proto}$ inertial load of the intended full-scale industrial platform. The construction of this physical prototype is discussed in the subsequent Chapter 4.

4

Mechanical Design, Fabrication and Avionics

This chapter presents the decisions regarding hardware and electronics for implementing a functional mechanism. The physical and dynamic limits of the selected test platform, the Holybro X500, influenced the structural architecture of the parallel-link mechanism. The core mechanism uses carbon fiber (CF) rods that extend 500 mm along the drone chassis. This extended projection, coupled with the payload, results in a significant forward shift of the global Center of Gravity. To safely conduct the parametric validation tests (0°, 15°, -15°, 30°) without saturating the primary flight controller, this static torque must be entirely compensated by the dual 1505-KV3750 tip actuators. A concurrent engineering approach was employed, in which tolerances and stress resistance of the 3D-printed linkages informed successive Computer Aided Design (CAD) iterations. The general workflow for designing a part, mentioned in the Delft Design Guide [9], starts with a simple 2D sketch in CAD. After sketching parts with rough dimensions and desired shapes, the structures were extruded into 3D shapes. Later, the parts are refined to include features such as holes, tolerances, and fillets. Figure 4.1 shows the fully assembled mechanism in Fusion360 CAD software [5].

The avionics-specific requirements needed to be factored into the part design and fabrication from the start. The mounting holes for motors and ESCs were planned based on the datasheet specifications, and the necessary clearances were provided for the wiring. The placement of the active tip actuators at the distal end requires extending high-current electronic power and control signals across the 500 mm longitudinal boom. This architecture must remain robust against mechanical vibrations while maintaining operational reliability throughout the flight test. A custom electronics and telemetry architecture was developed around the Holybro Pixhawk 6C Flight Management Unit (FMU). Because the system integrates a standard quadrotor lift mechanism with auxiliary tip motors, it requires specialized signal routing and control-allocation bypasses for flight testing. An overview of the power and signal flow is shown in Figure 4.6, and the mechanism with the assembled circuit is shown in Figure 4.7.

4.1. Additive Manufacturing and Material Selection

Following the finalization of the kinematic CAD model, the custom joint and mounting brackets were manufactured via Fused Deposition Modeling (FDM). The fundamental structures include the root link (which anchors the four-bar mechanism to the drone's baseplate) and the tip link (which houses the crossbar and motors).

Polylactic Acid reinforced with Carbon Fiber (PLA-CF) was selected as the primary filament due to its superior compressive strength [23], making it highly suitable for the dynamic load-bearing requirements of the brackets and motor mounts. The slicer parameters were optimized to maximize anisotropic strength and resist torsional shear forces generated by the tip rotors. The parts were printed with 6 perimeter walls and a 35% infill. The Gyroid internal geometry was specifically chosen to ensure multi-directional rigidity against both axial tension and lateral roll forces. For the less critical parts of source-detector mod-

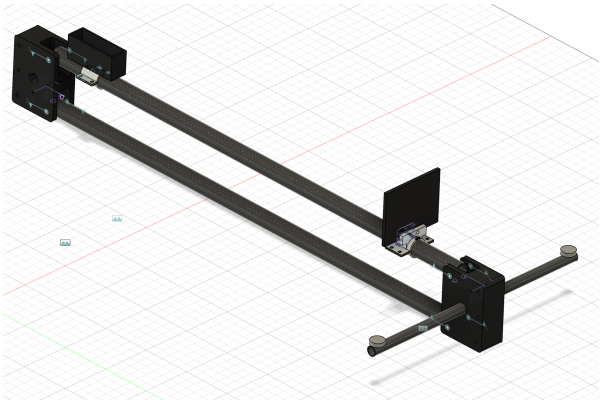


Figure 4.1: Full CAD of the manipulator mechanism

els and holders, where flexibility is not an issue, Polyethylene Terephthalate Glycol-modified (PETG) filament was used. All parts were optimally oriented on the print bed to minimize the need for support material, preserving dimensional accuracy on critical mating surfaces and bearing pockets. For connecting links, most examples in the literature used metal bars. However, for aerial application, where optimizing weight while maintaining considerable strength is essential, CF was chosen, particularly in tube form, due to its ease of availability and versatility.



Figure 4.2: Multiple progressive iterations of Root and Tip links

4.2. Structure Assembly

The base and tip links underwent multiple rapid iterations, as seen in 4.2, to refine the attachment tolerances and secure the parallel linkage. To establish a robust connection to the X500 attachment plate, the PLA-CF base link was retrofitted with brass threaded inserts as seen in Figure 4.3. These inserts were installed by heat staking, a process that uses thermal melting to locally reflow the thermoplastic, creating a permanent mechanical interlock upon cooling. This modularity allowed for rapid mounting and dismounting of the mechanism between flight tests.



Figure 4.3: Brass inserts fused into PLA

Securing the 3D-printed joints to the smooth 16 mm pultruded carbon fiber tubes poses a risk of struc-

tural failure and matrix delamination under flight vibration. In aerospace engineering, fastener placement in composite structures is governed by the Edge Distance Ratio (e/D), where e is the distance from the hole center to the free edge of the tube, and D is the hole diameter.

For carbon fiber matrices, the minimum recommended e/D ratio is $\geq$ 3.0 [1] to prevent mechanical tear-out. For this mechanism, using a $D = 3$ mm cross-pin, the minimum safe distance was calculated to be 9 mm (3.0×3 mm). To introduce a conservative safety margin against dynamic pitch loading, the edge distance was extended to 12 mm (4.0×3 mm). Specialized abrasive carbon fiber drill bits were used to precisely place these 3 mm cross-pin holes at the 12 mm mark, without compromising the structural integrity of the tube ends.

The structural assembly utilizes specific metric fasteners to secure the airframe components. M2x5 mm screws are used to mount the tip motors and propellers, while M3x10 mm screws fasten the root link and payload attachments. Longer M3x50 mm screws allow the CF rods to interface and pivot with both the root and tip links. Additionally, the crossbar is rigidly secured within the tip link cavity via an interference fit. The modular design of all the structures facilitated ease of packing and quick assembly at the drone lab at TU/e.

The 12 mm transverse CF crossbar housing the dual-tip actuators (Figure 4.4) required proper sizing. An excessively long bar amplifies the torsional leverage on the main boom's roll axis. In contrast, an overly short bar risks propeller collision with the tip link and induces severe aerodynamic interference between the overlapping tip vortices. To satisfy both constraints, the crossbar carbon fiber tubes were cut to a total span of 152 mm using a specialized abrasive saw. This specific geometry provides optimal horizontal clearance for the counter-rotating 4-inch propellers, ensuring clean airflow.

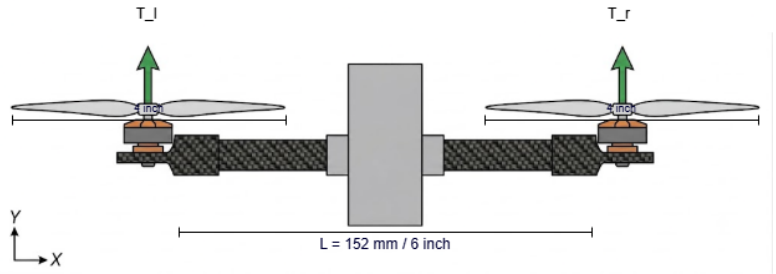


Figure 4.4: Front view of the transverse crossbar assembly, illustrating horizontal clearance for the 4-inch counter-rotating propellers

4.3. Payload Distribution

To safely validate the active control logic, the payload masses of the X500 prototype were scaled down to one-tenth of the intended full-scale heavy-lift application. The target mass distribution required 250 g loads on the CF rod around 100 mm and 350 mm, simulating detector and source models. To achieve an exact mass distribution without introducing volumetric bulk, standardized steel wheel-balancing blocks were used. These individual 5 g steel increments provided precise control over the mechanism's inertial properties. Up to 50 blocks were systematically stacked and secured to the 3D-printed payload structures, creating an accurate, highly dense physical representation of the theoretical distributed mass model as shown in Figure 4.5.

4.4. Actuation and Power Distribution

The tip motors were selected based on a systematic evaluation of the torque requirements under extreme conditions. Specifically, the thrust had to compensate for the source and detector prototype payloads at their maximum-leverage distances, with a conservative safety margin. Based on the static equilibrium Equation 3.5 calculated in Chapter 3, the required compensation thrust per motor was established at 205 g.

Initially, 1404 brushless motors were selected to provide this baseline, according to the datasheet, which should be able to handle the load at 50%. However, initial physical flight tests at $0°$-locked

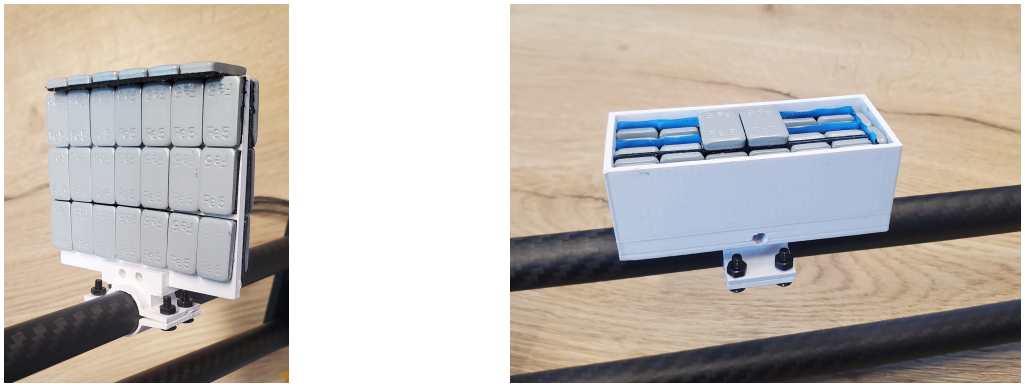


Figure 4.5: Models of Source and Detectors with weights

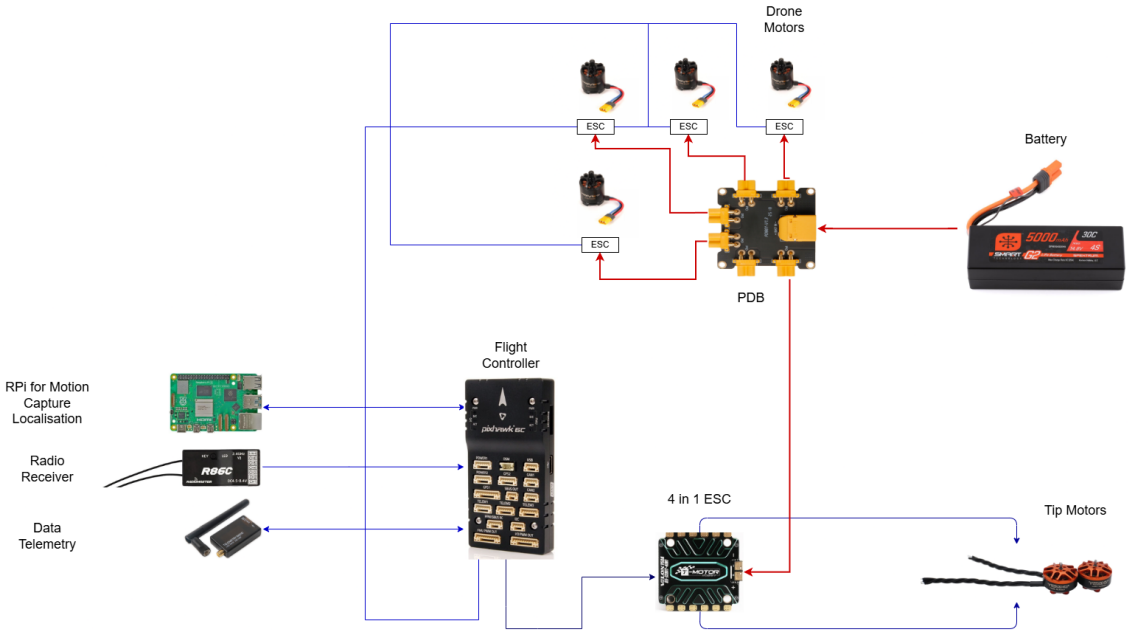


Figure 4.6: Signal and Power Flow diagram

pitch revealed a critical actuator limitation and a mismatch with the datasheet values. Overcoming unmodeled aerodynamic disturbances and the forward shift in the center of gravity required up to 85% manual throttle to manage a stable hover. This limits the available headroom, risking loss of control authority and inducing disturbances, as detailed in sub-chapter 7.2. Consequently, the actuators were upgraded to more efficient 1505 3750KV motors paired with 4-inch GF4024 propellers. According to the manufacturer's datasheet (Figure 4.8), this new configuration produces 206 g at 50% throttle and 281 g at 60% throttle. This upgrade restores the critical dynamic headroom needed to handle disturbances efficiently.

Power delivery to the dual motors is regulated by a T-Motor Velox V50A 4-in-1 Electronic Speed Controller (ESC). The motor datasheets indicate a peak current draw of 18.0 A under maximum load, which this ESC comfortably handles. More importantly, using a unified 4-in-1 ESC mitigates a structural threat of mechanical shudder and torsional roll-twist possibility in case of a discrete ESC malfunction. The 4-in-1 architecture ensures precise, simultaneous thrust control across the transverse crossbar. Centralizing the logic and power distribution reduces the complexity of phase-wire telemetry.

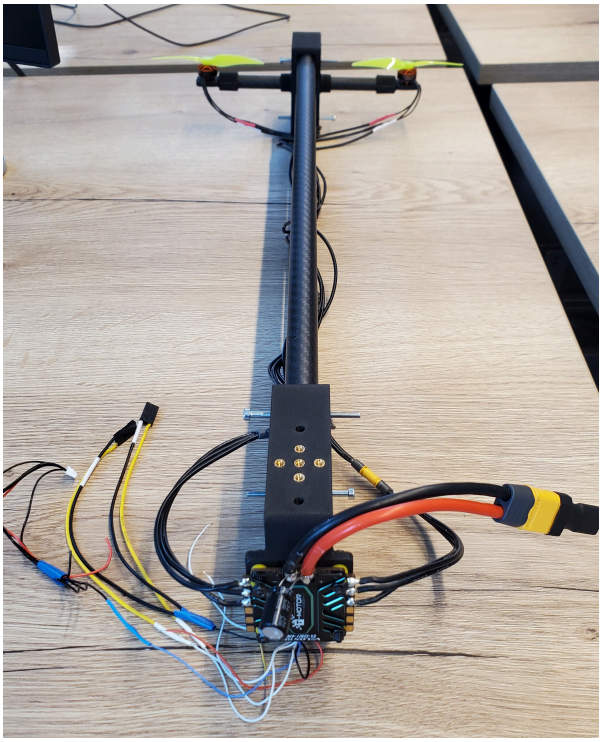


Figure 4.7: Fully assembled mechanism

4.5. Electronic Routing and Interconnects

Routing power from the chassis to the distal motors requires proper selection of conductor size to control voltage drop and prevent thermal overload along the extended boom. Based on the upgraded 1505 propulsion system, each motor is expected to draw a peak current of 18.0 A. Consequently, 18 AWG wire was selected as an appropriate compromise between current-carrying capability, electrical efficiency, weight, and routing flexibility. The resistance of 18 AWG copper wire is approximately 20.95 mΩ/m. With an estimated motor-to-ESC separation of 0.5 m, each motor phase conductor exhibits a resistance of:

$$R = (20.95 \times 10^{-3} \Omega/\text{m}) \times 0.5 \text{ m} = 0.0105 \ \Omega \tag{4.1}$$

Assuming the peak motor current of 18.0 A, the corresponding voltage drop and resistive power loss across a single conductor are:

$$V_{\text{drop}} = I \cdot R = 18.0 \text{ A} \times 0.0105 \ \Omega \approx 0.19 \text{ V} \tag{4.2}$$

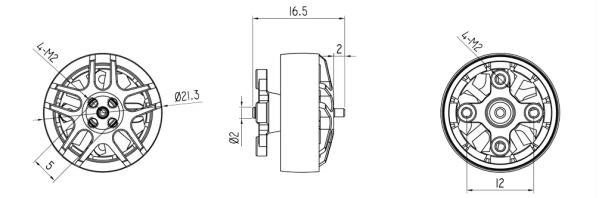
$$P_{\text{loss}} = I^2 \cdot R = (18.0 \text{ A})^2 \times 0.0105 \ \Omega \approx 3.4 \text{ W} \tag{4.3}$$

This resistive loss represents slightly over 1% of the nominal 4S LiPo battery voltage (≈ 16.8 V), and just over 5% of power consumed by the motor operating at 50% throttle, ensuring high electrical efficiency. Routing phase wires across the entire length of the motor and ESC connections required approximately 5 m of wiring. The selected 18 AWG conductors, therefore, provide sufficient current capacity while minimizing losses and preserving mechanical flexibility within the boom structure.

The critical electromechanical junction in the distal assembly is the connection between the ESC and the 1505 motors, requiring six individual phase connections. Direct soldering between the motor and ESC would be suboptimal; it prevents swapping in the event of motor failure or for a change in the motor's spin direction. MR30 three-pin connectors provided the needed modularity. These are natively compatible with 18 AWG wire, have low resistance (≈ 0.70 mΩ) and feature a mechanical lock that withstands flight vibrations. The motor leads were terminated with male MR30 pins, while the extended ESC power lines were terminated with female receptacles.

MOTORS: 1505-KV3750

Technical Datas	
KV	3750
Configu-ration	9N12P
Stator Diamter	21.3mm
Stator Length	9.5mm
Shaft Diameter	1.5mm
Motor Dimension(Dia.*Len)	Φ21. 3*16. 5mm
Weight(g)	11g
Idle current(10)@10V(A)	⩽ 0.6 A
No.of Cells(Lipo)	3-4S
Max Continuous Power(W)60S	200W
Internal Resistance	96 mΩ
Max Current(60S)	18A



Prop (inch)	Voltages (V)	Throttle (%)	Load Currency (A)	Power(W)	Pull(g)	Efficiency(g/W)	Temperature(in full throttle load 1min)
Prop (inch)	Voltages (V)	Throttle (%)	Load Currency (A)	Power(W)	Pull(g)	Efficiency(g/W)	Temperature(in full throttle load 1min)
GF3520	16.00	50%	3.6	57.6	195	3.39	64.6
		60%	5.2	83.2	253	3.04	
		70%	7.9	126.4	358	2.83	
		80%	10.4	166.4	434	2.61	
		90%	14.7	235.2	573	2.44	
		100%	16.6	265.6	590	2.22	
GF4024	16.00	50%	3.8	60.8	206	3.39	67.8
		60%	5.4	86.4	281	3.25	
		70%	8.7	139.2	365	2.62	
		80%	11.5	184.0	482	2.62	
		90%	15.3	244.8	573	2.34	
		100%	18.0	288.0	631	2.19	

Figure 4.8: Datasheet of 1505 KV3750 motors used for tip rotors

4.6. Telemetry and Control Bypass Architecture

The default flight controller for the X500 platform is the Pixhawk 6C, which natively allocates four ESC channels for the main quadrotor lift motors. The primary command link is maintained using a Radiomaster TX16S transmitter operating on the 2.4 GHz FrSky D16 LBT protocol, in compliance with European RF regulations. Drone reception is handled by a Radiomaster R88 V2 transceiver, configured to output a digital Serial Bus (SBUS) stream. To minimize latency, this SBUS output is routed directly to the Pixhawk's PPM/SBUS input terminal via a single-wire digital bus that carries all primary flight axes, mode selections, and auxiliary overrides.

Initial motor integration revealed a critical signal dependency; the Pixhawk 6C required uniform digital protocols across all auxiliary pins to successfully pass the pre-arming checks. Consequently, the ESC communication protocol was standardized to DShot, ensuring reliable telemetry and synchronous spool-up of the tip motors.

To perform the initial tests, the architecture required independent, manual throttle control of the tip actuators, entirely decoupled from the Pixhawk's primary attitude-stabilization loops. Software configurations were modified to bypass the standard PX4 Control Allocator, enabling direct radio control (RC) passthrough. This isolation strategy was configured via QGroundControl as shown in Figure 4.9.

This bypass architecture successfully isolates the experimental variables. It allows the operator to manually spool the tip motors to 205 g, establishing the AMC baseline before analyzing the main drone's log responses at varying parametric angles. (Depending on the experimental phase, this function can be toggled back to autonomous Motor 5/6 control when closing the loop).

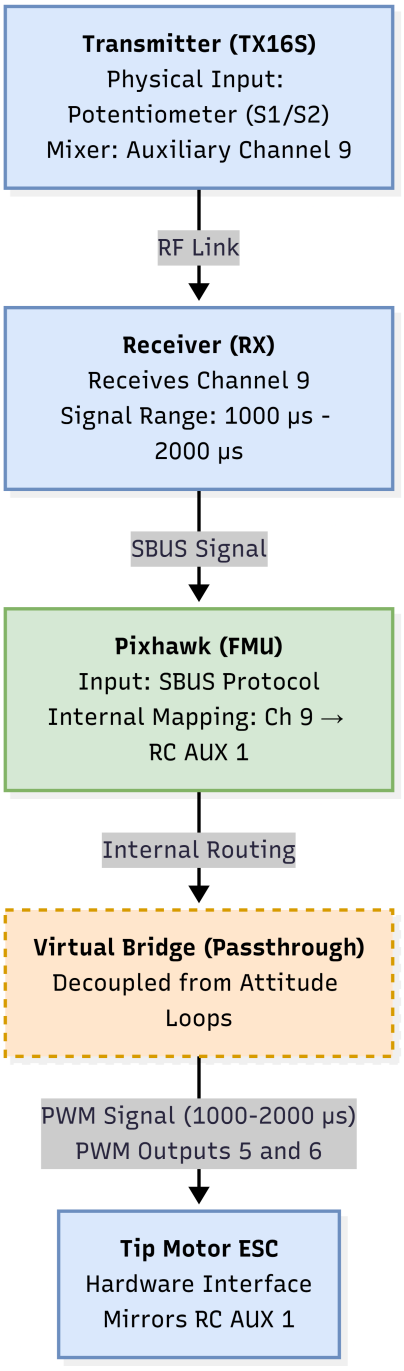


Figure 4.9: Passthrough configuration data flow

5

Control Architecture

This chapter explores the general control architecture of PX4 and its integration with the mechanism. To translate the AMC kinematics into physical flight, the mechanism relies on the robustness of the PX4 control architecture. While the 4-bar parallel link mechanism decouples the tip actuator vector from the boom angle, the aerial platform transitions from a standard 4-actuator multirotor into a coupled 6-rotor system. This chapter details the overall control architecture, focusing on how the PX4 Autopilot's Control Allocator (CA) is mathematically extended to manage redundant degrees of freedom and distribute the stabilization load between the primary lift rotors and the auxiliary tip rotors.

5.1. Cascade Control Architecture

The Unmanned Aerial Manipulator (UAM) utilizes a cascaded feedback control architecture inherent to the PX4 flight stack as seen in Figure 5.1. The architecture relies on a timescale separation between the slow translational dynamics and the fast rotational dynamics.

1. **Position Controller (Outer Loop):** Generates target velocity and thrust vectors based on GPS/Odometry feedback to maintain the spatial hover location.
2. **Attitude/Rate Controller (Inner Loop):** A high-frequency loop that compares the estimated attitude (from the extended Kalman filter) against the target attitude. It outputs normalized 3D torque demands (τ_x, τ_y, τ_z) and a collective thrust demand (F_z).
3. **Control Allocator (The Mixer):** The critical mathematical junction where the generalized 3D torque and 1D thrust demands are mapped to normalized, individual actuator commands ($u_1 ... u_6$).

5.2. Theoretical Formulation of the Control Allocator

In a standard quadrotor, the allocation matrix is square (and uniquely invertible) because there are four actuators mapped to four outputs (Roll, Pitch, Yaw, Thrust). The addition of the dual-tip rotors

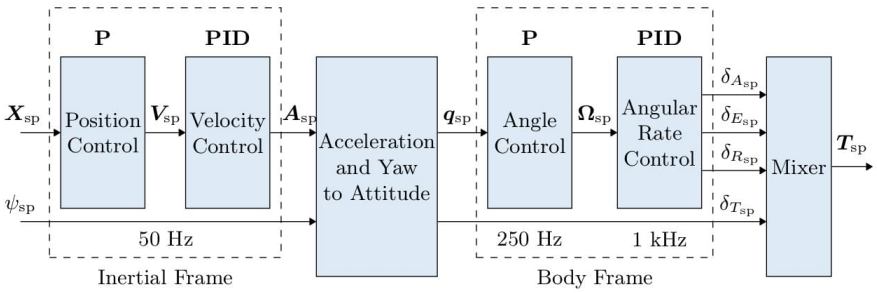


Figure 5.1: Multicopter control architecture block [30]

transforms the UAM into an overactuated system. The flight controller must algorithmically resolve how to achieve the demanded pitch torque using an optimal combination of the main frame rotors and the extended tip rotors.

The allocation problem is formulated as a linear mapping:

$$\boldsymbol{\nu} = \mathbf{B}\mathbf{u} \tag{5.1}$$

Where:

$\boldsymbol{\nu} = [\tau_x, \tau_y, \tau_z, F_z]^T$ is the vector of demanded torques and collective thrust.

$\mathbf{u} = [u_1, u_2, u_3, u_4, u_5, u_6]^T$ is the vector of normalized motor commands ($0 \leq u_i \leq 1$).

$\mathbf{B} \in \mathbb{R}^{4\times 6}$ is the Effectiveness Matrix, which encodes the specific geometric leverage of every actuator.

To incorporate the AMC architecture, the standard PX4 Effectiveness Matrix was extended. For any individual rotor i, its column in the $\mathbf{B}$ matrix is defined by its geometric position ($p_{x,i}, p_{y,i}, p_{z,i}$), its thrust vector alignment ($A_{x,i}, A_{y,i}A_{z,i}$), and its moment coefficient ($k_{m,i}$). Assuming a linearized thrust mapping where F_{max} represents the maximum thrust of an individual rotor, and assuming the auxiliary tip rotors ($i = 5, 6$) are aligned purely vertically ($A_x = A_y = 0$), the vertical offset p_z mathematically cancels out of the cross-product. Therefore, the columns for the auxiliary tip rotors are defined solely by their significant forward longitudinal offset, their lateral spacing, and their counter-rotating yaw moments:

$$\mathbf{B}_{boom} = \begin{bmatrix} p_{y,5} \cdot F_{max} & p_{y,6} \cdot F_{max} \\ -p_{x,5} \cdot F_{max} & -p_{x,6} \cdot F_{max} \\ k_{m,5} \cdot F_{max} & k_{m,6} \cdot F_{max} \\ A_{z,5} \cdot F_{max} & A_{z,6} \cdot F_{max} \end{bmatrix} \tag{5.2}$$

Because the system is over-actuated ($\mathbf{B}$ is non-square), a unique solution for $\mathbf{u}$ does not exist. The PX4 Control Allocator resolves this by computing the Moore-Penrose pseudo-inverse ($\mathbf{B}^+$) to find the minimum-norm actuator commands that satisfy the demanded moments

$$\mathbf{u} = \mathbf{B}^+\boldsymbol{\nu} \tag{5.3}$$

By explicitly embedding the forward offset of the tip rotors into the $\mathbf{B}$ matrix, the Control Allocator mathematically models that Actuators 5 and 6 possess high pitch authority. When the forward-shifted Center of Gravity (CoG) generates a static nose-down torque during flight, the pitch rate controller detects the resulting steady-state error, and its integral winds up, demanding a continuous compensating pitch-up torque. Because of this updated $\mathbf{B}$ matrix, CA's pseudo-inverse algorithm efficiently fulfills this demand by biasing the thrust allocation heavily toward the tip-motors. This achieves Active Moment Compensation without requiring a separate, custom-coded PID loop, relying instead on the seamless integration between the native rate controllers and the updated physics-based control allocation pipeline.

5.3. Dual-Mode Control Strategy for Parametric Validation

While closed-loop flight utilizing the integrated 6-rotor allocation scheme is the desired end-state controller, applying it immediately would overlook aerodynamic phenomena, such as cross-axis coupling and structural tension. To better isolate and study these effects during the parametric validation at $0°$,$\pm 15°$, $30°$, this thesis employs a dual-mode control strategy. These strategies were based on the architectures from the literature as discussed in 2.2.

Mode 1: Open-Loop Passthrough (Isolated AMC)

In this mode, the PX4 Control Allocator is reduced to a 4×4 allocation matrix, effectively ignoring the two boom-mounted tip rotors. An SBUS radio control (RC) bypass is used to map a transmitter potentiometer directly to the auxiliary ESC PWM outputs.

This configuration isolates the AMC system from the PX4 attitude controller. By manually adjusting the tip motors until the vehicle reaches a level hover, the static thrust required to maintain equilibrium and

the onset of actuator saturation can be measured experimentally without interference from the flight controller.

Mode 2: Closed-Loop Active Allocation

In this mode, the complete 4×6 pseudo-inverse control allocation matrix is enabled, allowing the PX4 flight controller to command all six motors simultaneously. The transmitter can function in default settings without any switch mapping.

This configuration is used to evaluate the competence of the $\mathbf{B}$ allocation matrix. Any differences between the predicted control allocation and the observed flight response, such as steady-state pitch errors or integrator windup, indicate dynamics that are not captured by the model. These may include aerodynamic interference, structural effects, or cross-axis coupling at different boom angles.

6

Simulation

This chapter presents the details of the mechanism's experimental setup in the simulation environment and the results obtained. The extended beam mechanism introduces a severe center-of-gravity (CoG) offset. Without active compensation from the tip rotors, the quadcopter might exhibit an uncontrollable pitch moment during hover. Consequently, validating the active compensation architecture in a risk-free environment was essential before deploying physical hardware.

Following the preliminary CAD phase, we constructed a high-fidelity Software-in-the-Loop (SITL) digital twin to evaluate the manipulator's static moment balance. This simulation stack couples the Gazebo physics engine with the PX4 Autopilot flight stack, orchestrated via a ROS 2 Humble [17] launch infrastructure. To establish this environment efficiently, the existing ROS package, originally developed by TU/e and SpectX for X-ray inspection simulations, was repurposed by replacing the legacy gimbal attachment architecture with a custom parallel-link mechanism.

The primary engineering challenge within this digital twin was integrating the tip actuators into the PX4 Control Allocator (CA) module. To achieve this, the simulation environment was engineered to satisfy the following criteria:

1. *Rigid-Body Modeling*: Model the complete rigid-body dynamics of the drone, arm, and rotor assembly using CAD-derived inertial properties.
2. *Aerodynamic Calibration*: Analytically calibrate the tip rotors aerodynamic parameters directly from motor-propeller datasheet curves.
3. *Dual-Mode Architecture*: Provide a configurable control architecture that permits both PX4-integrated and independent ROS 2 control of the tip motors.
4. *Control Allocation Extension*: Extend the PX4 Control Allocator from a standard 4-motor quadrotor to a custom 6-motor geometry, allowing the autopilot's primary attitude controller to command the tip motors directly.

6.1. PX4-ROS-Gazebo Architecture

The simulation environment is built upon a tripartite architecture: Gazebo Harmonic handles the rigid-body physics and aerodynamic rendering, PX4 Autopilot manages the flight controller firmware and control allocation, and ROS 2 Humble orchestrates inter-process communication. The digital twin is built using a hierarchical XACRO architecture. It links the base X500 quadrotor frame to the arm's inertial links, with a conditional flag to include the dual 1404 3850KV tip rotors. To prevent coordinate mismatches, all spatial coordinates are properly aligned between Gazebo's Forward-Right-Down (FRD) convention and PX4's native North-East-Down (NED) body-fixed frame. The tip rotors are positioned at $(+0.678, \pm 0.12, -0.045)$ m relative to the global Center of Gravity, aligning them perfectly with the end of the mechanism rods. The complete system architecture is illustrated in Figure 6.1.

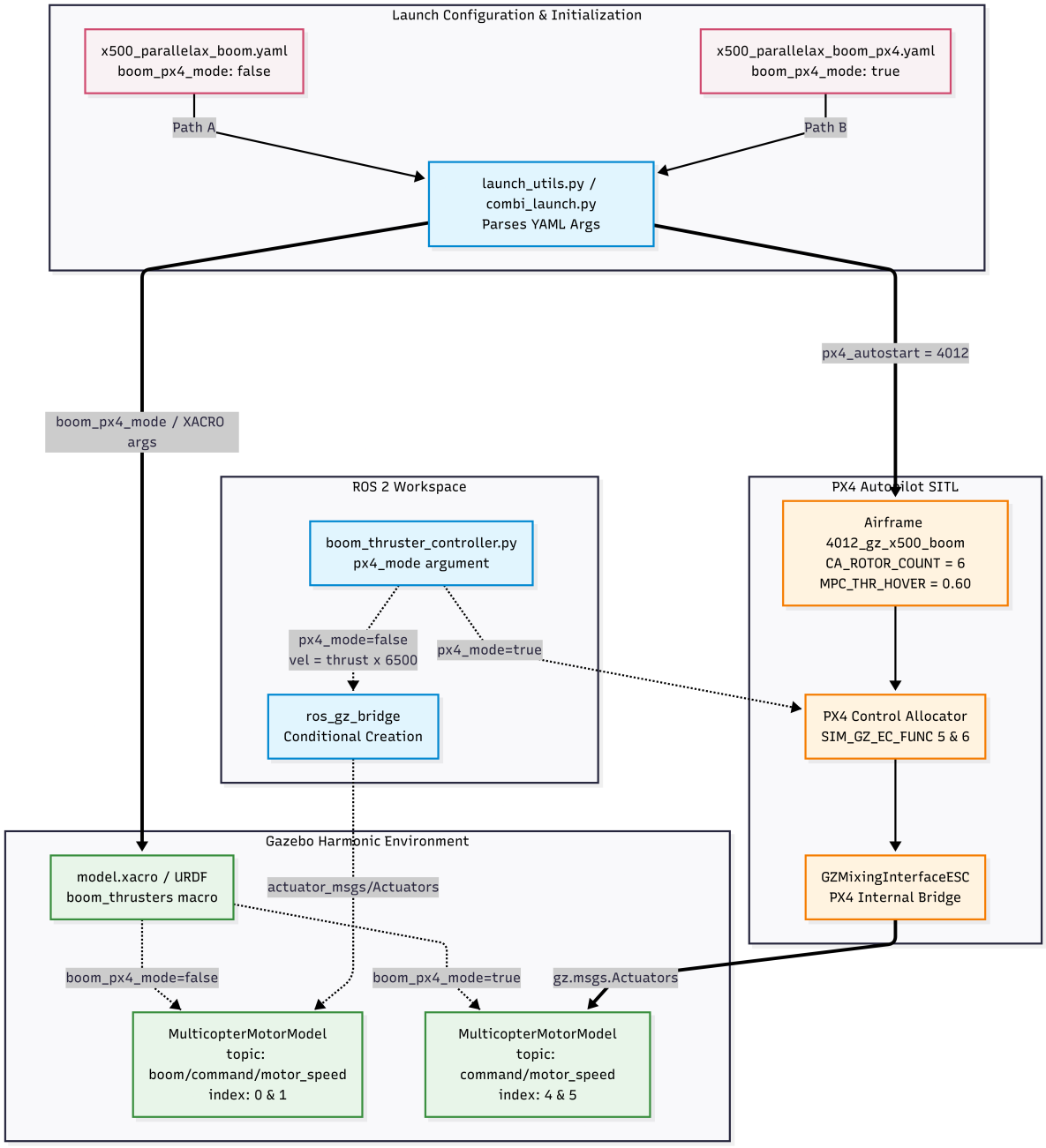


Figure 6.1: System architecture and dual-mode signal routing. Mode 1 utilizes a dedicated ROS 2 bridge for isolated ground testing, while Mode 2 fully integrates the 6-motor geometry (Airframe 4012) into the PX4 Control Allocator via the internal GZMixingInterfaceESC

6.2. Rotor Integration and Mathematical Calibration

To ensure accurate simulation, the inertial properties were rigorously mapped from the Fusion 360 CAD assembly. The rigid arm geometry was imported as an STL mesh (base_link.stl) and scaled accordingly. To align the CAD's longitudinal axis with the body-frame X-axis, a -90° yaw rotation was applied to the visual origin. Crucially, because the CAD environment utilized a Y-forward convention, the inertia tensor was mathematically transformed via a 90° rotation about the Z-axis to match the Gazebo X-forward frame:

$$I_{body} = R_z(-90^\circ) \cdot I_{CAD} \cdot R_z(-90^\circ)^T \tag{6.1}$$

This transformation accurately swaps the I_{xx} and I_{yy} principal moments while mapping the off-diagonal I_{yz} term to I_{xz}. The resulting arm mass, with all payloads and links attached, is 728 g in Fusion 360 (which accurately aligns with the actual physical weight of 732 g), representing approximately 27% of the total vehicle mass and inducing a forward CoG offset (≈8 cm) that drives the active compensation requirement. By decoupling the visual origin from the inertial center of mass, the simulation easily accommodates translational shifts to test various physical mounting configurations without altering the underlying mesh. Iterative adjustments verified the proper alignment of the links relative to the physical prototype.

The simulation fidelity relies on the accuracy of the Gazebo MulticopterMotorModel plugin, which governs the following equations:

Thrust:

$$F = k_T \cdot \omega^2 \tag{6.2}$$

Reaction torque:

$$\tau = k_m \cdot F = k_m \cdot k_T \cdot \omega^2 \tag{6.3}$$

Motor dynamics (first-order lag):

$$\dot{\omega} = \frac{1}{\tau_{up/down}}(\omega_{cmd} - \omega) \tag{6.4}$$

where ω is the angular velocity in rad/s, ω_{cmd} is the commanded velocity, and τ_{up}, τ_{down} are the spin-up and spin-down time constants respectively. The parameters for the dual 1404 3850KV tip rotors with GF4024 propellers at 16.0 V were derived directly from the manufacturer's shaft-power analysis.

The mechanical shaft power P_{mech} is derived by subtracting the copper (I^2R) and estimated iron losses from the electrical input power [11] at the 60% throttle operating point:

$$P_{\text{mech}} = VI - I^2R - (V_{\text{idle}}I_{\text{idle}}) = 118.4 - 7.78 - 6.0 \approx 104.7 \text{ W} \tag{6.5}$$

Accounting for an under-load speed droop factor $\eta_{\text{slip}} = 0.75$, the rotational shaft speed ω_{real} and resulting torque τ are calculated as:

$$\omega_{\text{real}} = K_V \cdot V \cdot \delta \cdot \eta_{\text{slip}} \cdot \frac{2\pi}{60} \approx 2902 \text{ rad/s} \tag{6.6}$$

$$\tau = \frac{P_{\text{mech}}}{\omega_{\text{real}}} = \frac{104.7}{2902} \approx 0.0361 \text{ N} \cdot \text{m} \tag{6.7}$$

Given a measured thrust $F = 2.315$ N at 60% throttle, the moment constant k_m (torque-to-thrust ratio) is:

$$k_m = \frac{\tau}{F} = \frac{0.0361}{2.315} \approx 0.016 \text{ m} \tag{6.8}$$

For the simulation plugin (following the default PX4 convention of $\omega_{\text{max,sim}} = 1000$ rad/s), the thrust constant $k_{T,\text{sim}}$ at the 45% throttle hover point ($F_{\text{hover}} = 1.834$ N) and the corresponding rotor drag coefficient C_{drag} are defined as:

$$k_{T,\text{sim}} = \frac{F_{\text{hover}}}{(\delta_{\text{hover}} \cdot \omega_{\text{max,sim}})^2} \approx 9.2 \times 10^{-6} \tag{6.9}$$

$$C_{drag} = k_m \cdot k_{T,\text{sim}} = 0.016 \times 9.2 \times 10^{-6} \approx 1.47 \times 10^{-7} \tag{6.10}$$

Table 6.1: Overview of the Calibrated Parameters

Parameter	Symbol	Value	Unit
Thrust coefficient	k_T	9.2×10^{-6}	N·s^2/rad^2
Moment coefficient	k_m	0.016	m
Rotor drag coefficient	C_{drag}	1.47×10^{-7}	N·m·s^2/rad^2
Spin-up time constant	τ_{up}	0.008	s
Spin-down time constant	τ_{down}	0.025	s
Maximum angular velocity	ω_{max}	1000	rad/s
Rotor mass (motor + prop)	m_r	0.0115	kg
Rotor inertia (about spin axis)	I_{zz}	1.9×10^{-6}	kg·m^2

The complete calibrated parameter set is summarised in table 6.1.

The spin-up time constant (0.008 s) is significantly shorter than that of the main rotors (0.0125 s), reflecting the lower inertia and higher KV rating of the 1404 motor compared to the 5010-920KV main motors.

The tip rotor inertia was accurately scaled from the known X500 main rotor values using a mass-ratio and radius-ratio approach:

$$\begin{aligned} I_{boom} &= I_{main} \times \frac{m_{boom}}{m_{main}} \times \left(\frac{r_{boom}}{r_{main}}\right)^2 \\ I_{boom} &= 2.65 \times 10^{-5} \times \frac{0.0115}{0.016} \times \left(\frac{0.051}{0.165}\right)^2 \approx 1.9 \times 10^{-6} \text{ kg} \cdot \text{m}^2 \end{aligned} \tag{6.11}$$

where $r_{boom} = 0.051$ m (4-inch propeller radius) and $r_{main} = 0.165$ m (13-inch propeller radius).

The drone in the simulation environment, with the mechanism attachment and tip rotors, is shown in Figure 6.2.

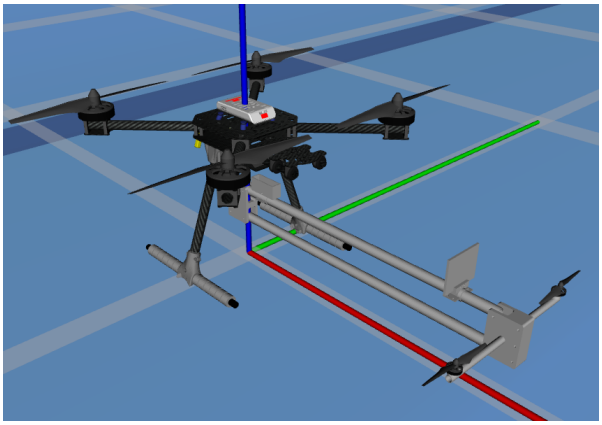


Figure 6.2: X500 drone with parallelax mechanism of additional tip propellers in RViz

6.3. PX4 Control Allocator Extension

The PX4 Control Allocator mathematically resolves the abstract torque and thrust setpoints generated by the attitude rate controller into normalized, individual motor commands. While the standard X500 airframe (PX4 ID 4001) relies on a rigidly defined 4-rotor effectiveness matrix, this topology is insufficient for an over-actuated system. Therefore, building upon the theoretical framework established in Section 5.2 earlier, a custom 6-rotor airframe configuration was implemented to explicitly embed the tip-rotors as controllable actuators within the primary attitude loop.

By extending the base multirotor geometry to include the forward and lateral geometric offsets of the distal motors (modifying the `CA_ROTOR_*` parameters in the airframe file), the Control Allocator's Moore-Penrose pseudo-inverse solver can automatically compute the optimal thrust allocation across all six motors. This enables the flight stack to dynamically treat the tip-rotors as pitch-compensation actuators without requiring external ROS 2 override commands.

6.4. Dual-Mode Control Architecture for Simulation

The control software was developed and validated in progressive stages. Actuator control compensation was first tested in isolation to bypass the overhead of the full PX4 flight stack. Upon functional verification, the control logic was integrated into the PX4 architecture and expanded to support two mutually exclusive operating modes, as discussed in 5.3.

Mode 1 - Independent ROS 2 Control (Open-Loop)

The tip motor plugin subscribes to a dedicated Gazebo topic, `boom/command/motor_speed`, separate from the main rotor command topic, and drives the motors directly via velocity commands from custom ROS 2 nodes. PX4 operates with the standard 4-motor geometry (airframe 4001) and is unaware of the tip rotors. This mode isolates the motor thrust compensation from the drone's internal PID loops, serving as a baseline for characterizing the mechanism's thrust authority.

Mode 2 - PX4 Control Allocator Integration (Closed-Loop)

In this mode, the boom motor plugins share the same `command/motor_speed` topic as the main rotors. PX4 operates with a custom 6-motor geometry (airframe 4012) and the Control Allocator actively commands all six motors through its attitude control loop. The Control Allocator automatically computes the optimal thrust allocation across all six motors to satisfy the demanded torques and thrust, enabling the tip rotors to provide active pitch compensation for the arm-induced CoG offset. The actuator settings page of QGroundControl software (Figure 6.3) confirms the updated airframe file.



Figure 6.3: The custom airframe 4012 configuration displayed in QGroundControl software

6.5. Validation

The Digital Twin simulation was validated through Closed-Loop flight testing (Mode 2) in a local Ubuntu 22.04 environment powered by a GTX 1650. The Gazebo physics engine maintained a highly efficient average Real-Time Factor (RTF) of 0.95. This computational performance ensures that the high-frequency motor dynamics, specifically the 0.008 s spin-up time constant of the 1404 tip motors, were accurately simulated without physics step-clipping.

During simulated arming, all six motors successfully achieved synchronous idle speeds. In flight, the Control Allocator successfully leveraged the expanded matrix to autonomously command higher sustained thrust from the distal rotors, thereby counteracting the forward CoG offset. The vehicle achieved

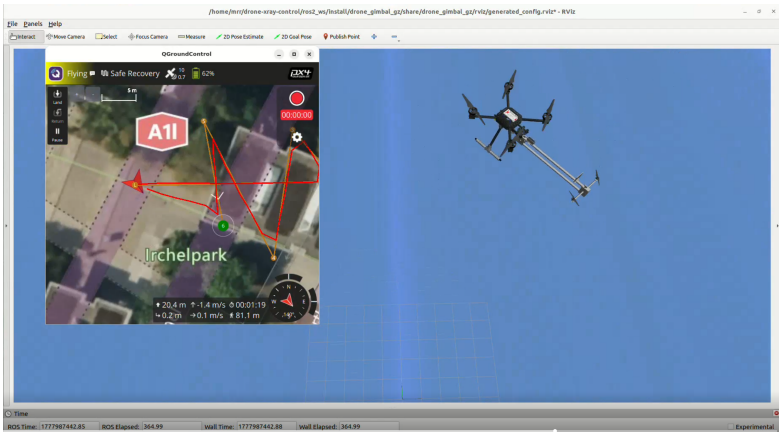


Figure 6.4: Drone in tracing the simulated flight path accurately with the functional tip rotors

a highly stable hover and accurately tracked the simulated flight paths (Figure 6.4). Later attempts were made to implement the movable parallel linkage within the simulation environment. However, this revealed a critical limitation of the URDF representation in handling cyclic joints, and it was deemed more efficient to prototype the parallel linkage in hardware.

Mode 2 flight tests successfully validated the preliminary AMC architecture, confirming the thrust authority of the tip rotors and effectively de-risking upcoming physical flight tests. While these simulations cannot capture every nuance of real-world hardware, this phase was vital for verifying the control logic and building the core codebase, which ultimately required only minor adjustments prior to physical deployment.

7

Experimental Validation (Flight Tests)

In this chapter, the real flight experiments with the mechanism and the results are discussed in detail. Following the Software-in-the-Loop (SITL) simulations, physical flight trials were conducted within the controlled flight arena at the Eindhoven University of Technology (TU/e) Drone Lab. The objective of this experimental phase was to empirically validate the theoretical Active Moment Compensation architecture and evaluate the system's structural and kinematic responses.

To isolate the variables of static torque, thrust headroom, and cross-axis coupling, the experimental methodology was structured as a discrete parametric sweep. The parallel manipulator mechanism was mechanically locked at four distinct kinematic states: $\theta = \{0°, 15°, -15°, 30°\}$. The flight tests first evaluate Open-Loop (manual RC passthrough), then focus on the Closed-Loop (Control Allocator-driven) architecture to map the control boundaries of the tip rotors. The quantitative data, including Root Mean Square Errors (RMSE) for attitude tracking, and tip motor headroom margin (H_m), extracted from the PX4 messages in the logs, are compiled in the Table 7.1. It is important to note that the initial and final seconds of the graphs capture the transient dynamics of takeoff and landing, where the uncompensated payload induces a severe pitch-forward moment. To ensure rigor, the RMSE data compiled in Table 7.1 strictly bounds the stable flight phase, excluding these transient takeoff and landing spikes.

7.1. Phase 1: System Integration and Open-Loop Baseline ($\theta = 0°$)

Before autonomous flight, the mechanism's electromechanical integrity was verified via Open-Loop manual control, in which the boom-mounted tip rotors are independent of the PX4 flight controller's internal stabilization logic.

Initial flight tests were conducted with the parallel link mechanism fixed at $\theta = 0°$, without the simulated source and detector masses to establish a baseline (FT-01). Using the manual RC passthrough, stable hover was achieved at approximately 30% throttle input, maintaining a tightly bounded Pitch RMSE of $0.556°$. This result empirically validated the baseline structural mass of the carbon fiber components (m_{boom}) and verified the 4-in-1 ESC signal synchronization.

Subsequently, masses were introduced for flight test under loaded conditions (FT-02). The source and detector masses, each 220 g, were fixed at the designated distances of 100 mm and 350 mm from the pivot point. Under Open-Loop control, achieving a level hover required a manual tip-rotor throttle input of approximately 85%. Figure 7.1, where the AUX2 rotary switch, plotted in blue, mapped from -1 to 0, controls the input transmitted to the tip rotors.

While stable vertical flight was achieved, an 85% static throttle limits the dynamic headroom margin, as established in Equation 3.6 from Chapter 3. With only 15% of thrust capacity remaining, the tip-motors lacked the control authority to handle disturbances. The telemetry from FT-02 reflects this: Yaw Rate RMSE spiked to $12.59°/s$. This limited control authority may explain the observed yaw-axis instability during liftoff.

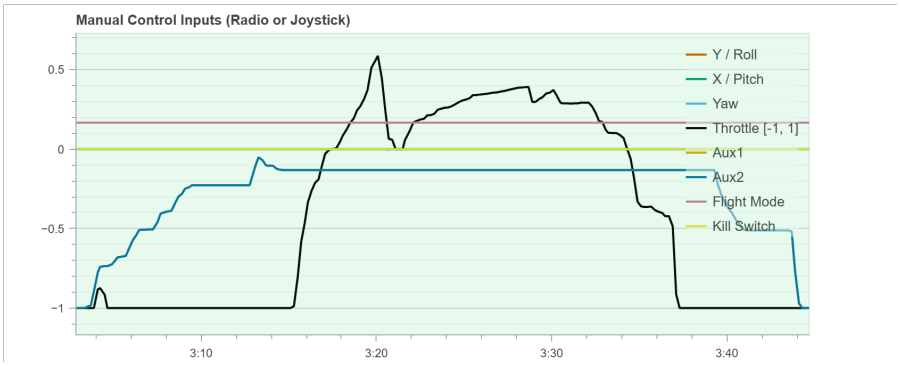


Figure 7.1: Plot showing steady state throttle input close to 85% needed for stable flight

7.2. Phase 2: Closed-Loop Autonomous Evaluation ($\theta = 0°$)

Following the manual baseline, the custom 6-motor airframe geometry is loaded as the Pixhawk 6C's airframe. This allows the Control Allocator to incorporate the tip-rotors into the control effectiveness matrix, enabling it to distribute commanded torques across all six rotors as part of the PX4 flight controller's internal stabilization logic.

In the unloaded configuration (FT-03), the drone achieved a highly stable, smooth flight envelope across all axes, with no manual RC input to the tip rotors. The Rate Controller's integral loop computed the compensating torque needed to nullify the forward Center of Gravity (CoG) shift, which the Control Allocator then mapped to the appropriate thrust distribution across the rotors.

Despite the visually stable flight performance, post-flight telemetry analysis of the unloaded test revealed a persistent steady-state error between the Pitch Estimated (actual attitude) and the Pitch Setpoint (demanded attitude), yielding a Pitch RMSE of $7.76°$, as illustrated in Figure 7.2.

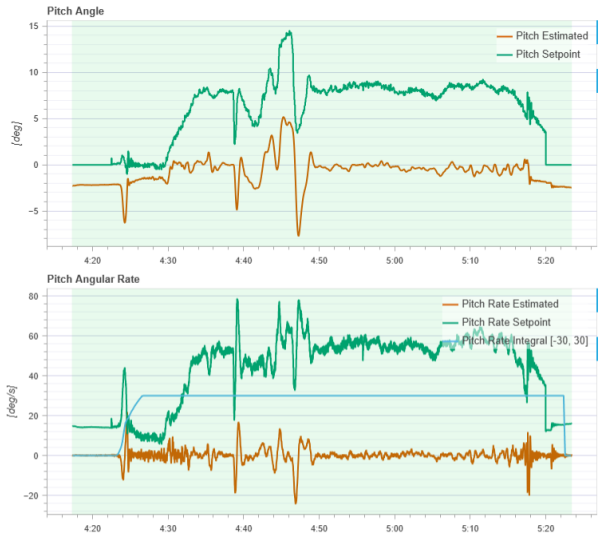


Figure 7.2: Pitch Estimated vs Setpoint offset obtained from logs

This offset indicates a physical discrepancy between the drone's actual CoG and the geometric center assumed by the control allocation geometry. Because the drone was visually stable but mathematically offset, the I-term (Integral) of the pitch rate controller continuously wound up to counter a static mechanical imbalance, generating a correcting torque that the baseline feedforward model cannot inherently predict.

For the next test, when a 440 g total payload was reintroduced under Closed-Loop control (FT-04), the system failed to lift off, exhibiting severe yaw translation around the landing gear, forcing an abort. Post-flight analysis of the Actuator Outputs (Figure 7.3) revealed a critical divergence in the tip rotor

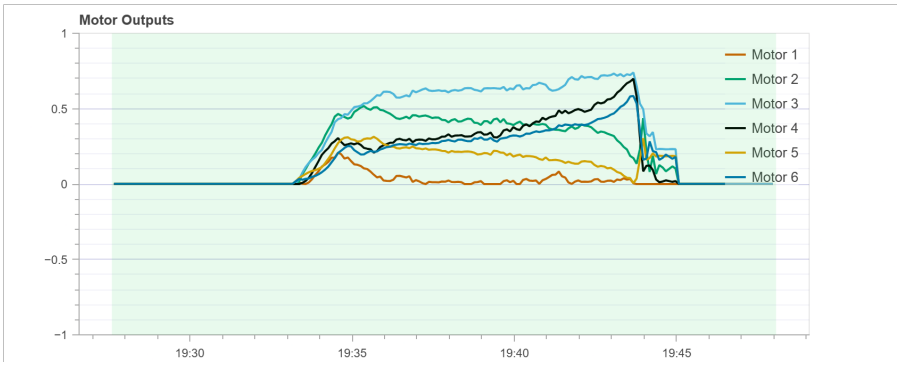


Figure 7.3: Motor outputs of the drone under full weight with 1404 motors

commands: the signal to Motor 6 spiked to a high output, while Motor 5 dropped unexpectedly low. This failure prompted verification of the default values for all motor-related parameters. Also, given the limited capability of 85% static thrust requirement to manage the massive pitch torque and stabilize the roll/yaw axes simultaneously, it was deemed appropriate to upgrade the tip motors for the subsequent tests.

7.2.1. System Upgrade and Parameter Resolution

To overcome the 85% throttle requirement limitation observed with the 1404 motors, the tip motors were upgraded to the 1505 3750KV motors on the next flight test day. During the initial tests with zero load (FT-05), there was noticeable difficulty taking off and controlling the drone with the mechanism. Logs revealed a massive Pitch RMSE of $20.85°$ and a Pitch Rate RMSE of $134.56°/s$. Analysis revealed an impending issue in the custom 6-rotor mixing geometry: the default PX4 Control Allocator assumes all rotors have identical thrust profiles and coefficients.

According to the motor datasheets, the AIR2216II main rotors with 10-inch propellers produce a maximum thrust of *1332 gf*. Conversely, the upgraded 1505 tip motors with 4-inch propellers deliver a maximum thrust of *631 gf*. To correct this thrust asymmetry in the software, the thrust coefficient parameters for the tip rotors (`CA_ROTOR4_CT` and `CA_ROTOR5_CT`) were remapped. By linearly scaling the coefficient from the default value of 6.5 to 3.0, the Control Allocator was informed of the reduced thrust authority at the airframe's tip. Following this parameter update (FT-06), the unloaded flight control improved drastically, and the Pitch RMSE plummeted to just $0.885°$ (Figure 7.4). This convergence of Estimated and Setpoint values held across unloaded tests locked at $\pm 15°$ and $30°$, as shown in Figure 7.5.

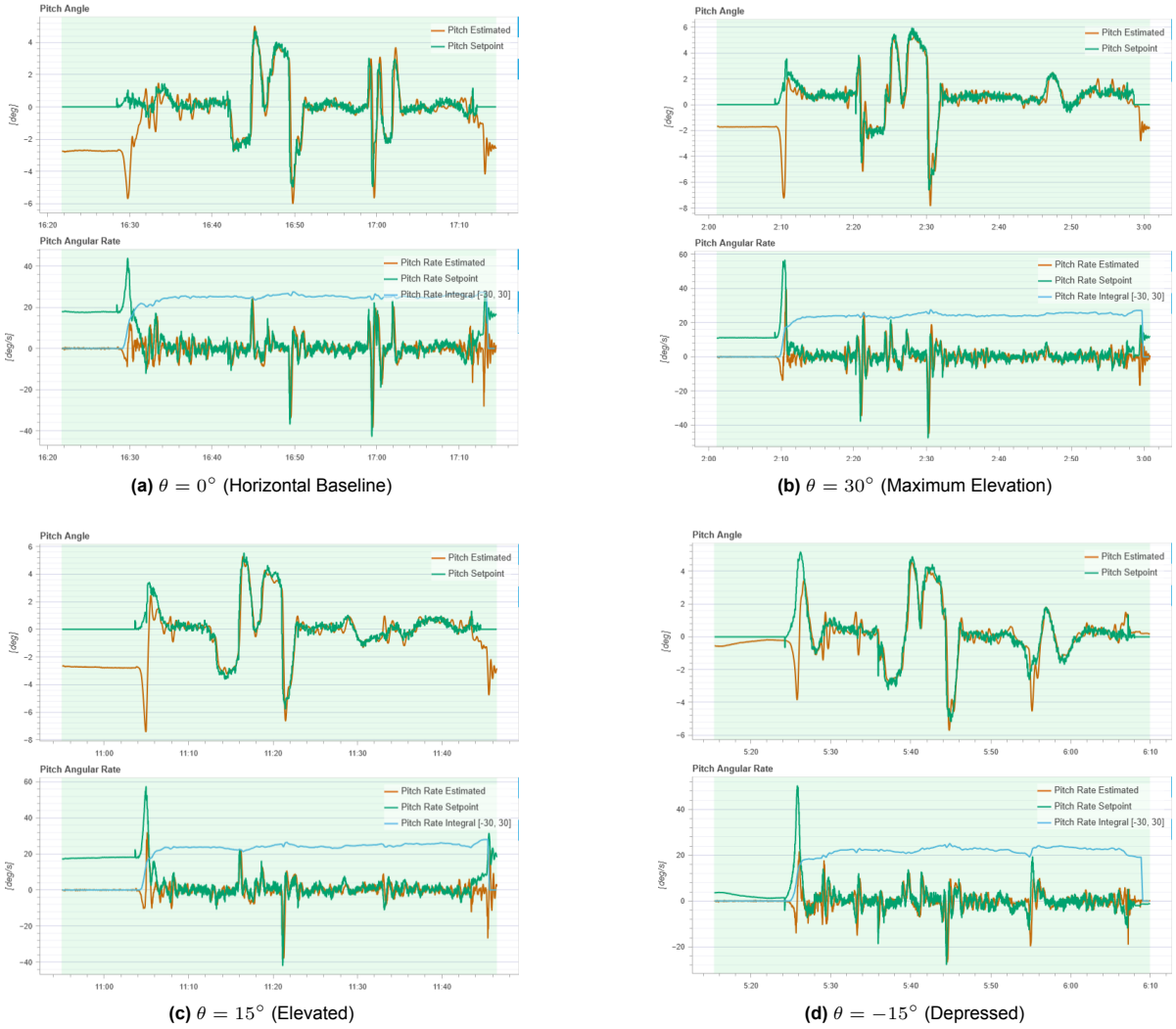


(a) Before changing CA_ROTOR_CT parameter



(b) After changing CA_ROTOR_CT parameter

Figure 7.4: Plot of Pitch Angle and Pitch Angular Rate



(a) $\theta = 0°$ (Horizontal Baseline)

(b) $\theta = 30°$ (Maximum Elevation)

(c) $\theta = 15°$ (Elevated)

(d) $\theta = -15°$ (Depressed)

Figure 7.5: Plots of Pitch Angle and Angular rates at parametric θ angles under no load

7.2.2. The Loaded Anomaly: Unmodeled CoG Translation

Subsequent closed-loop flight testing of the 1505 motors was carried out progressively: first at half load (250 g, FT-07), then at full payload (500 g, FT-10). Post-flight test log evaluation confirmed that the tip motors successfully handled the full load, operating at an efficient 50.3% average dynamic headroom margin ($H_m\%$) and maintaining a stable hover across the kinematic states (Figure 7.6). This demonstrated that the upgraded mechanism had sufficient dynamic headroom to manage cross-axis coupling without risking control saturation.

However, despite the tip rotors successfully maintaining the active moment, the introduction of the payload caused the steady-state pitch offset to abruptly reappear, with Pitch RMSE jumping from $0.88°$ (unloaded) to $13.11°$ (500 g load).

The re-emergence of this anomaly highlights a limitation in the default flight controller architectures. While the tip actuators effectively cancel the static gravitational torque ($\tau_g = \tau_{thrust}$) to prevent the drone from pitching over, they cannot alter the physical mass distribution. Adding 500 g along the 500 mm boom physically translates the Center of Gravity (CoG) significantly forward ($+\Delta x_{cg}$). As illustrated in the PX4 actuator control pipeline Figure 7.7, the Control Allocation (CA) module computes specific motor commands based on a rigid, hardcoded geometry matrix, assuming the CoG remains perfectly aligned with the geometric center of the primary quadrotor frame.

To mathematically define this tracking error, let m_{base} represent the mass of the unloaded X500 chassis and m_{load} represent the 500 g payload located at the projection distance L_{boom}. The forward translation

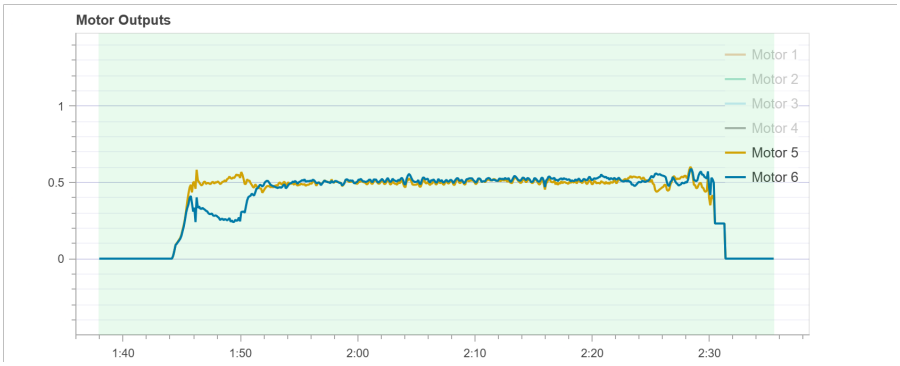


Figure 7.6: 1505 motor output while balancing a full load of 500 g

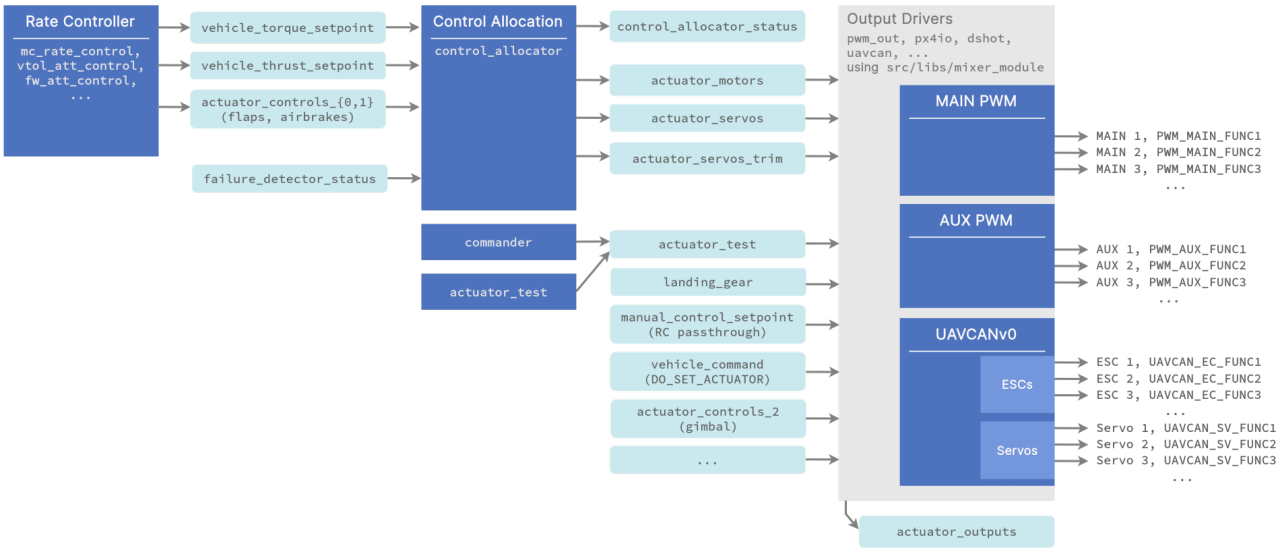


Figure 7.7: Overview of the Mixing Pipeline [29]

of the physical CoG (Δx_{cg}) along the longitudinal axis is defined as:

$$\Delta x_{cg} = \frac{m_{load} \cdot L_{boom}}{m_{base} + m_{load}} \tag{7.1}$$

When mapping the commanded pitch torque setpoint ($\tau_{y,soft}$) to the main quadrotor lift motors, the CA assumes symmetrical longitudinal moment arms (l_x) for both the front and rear rotors. If T_{front} and T_{rear} represent the combined thrust of the front and rear main rotor pairs, the software anticipates the resulting physical pitch torque to be:

$$\tau_{y,soft} = l_x(T_{front} - T_{rear}) \tag{7.2}$$

However, because the physical CoG is translated forward by Δx_{cg}, the true rotational pivot point of the drone has shifted. The physical moment arm of the front rotors is reduced to $(l_x - \Delta x_{cg})$, while the rear rotors' moment arm is extended to $(l_x + \Delta x_{cg})$. The actual physical pitch torque ($\tau_{y,phys}$) exerted on the airframe is:

$$\tau_{y,phys} = (l_x - \Delta x_{cg})T_{front} - (l_x + \Delta x_{cg})T_{rear} \tag{7.3}$$

Expanding this equation reveals the exact source of the tracking anomaly:

$$\tau_{y,phys} = l_x(T_{front} - T_{rear}) - \Delta x_{cg}(T_{front} + T_{rear}) \tag{7.4}$$

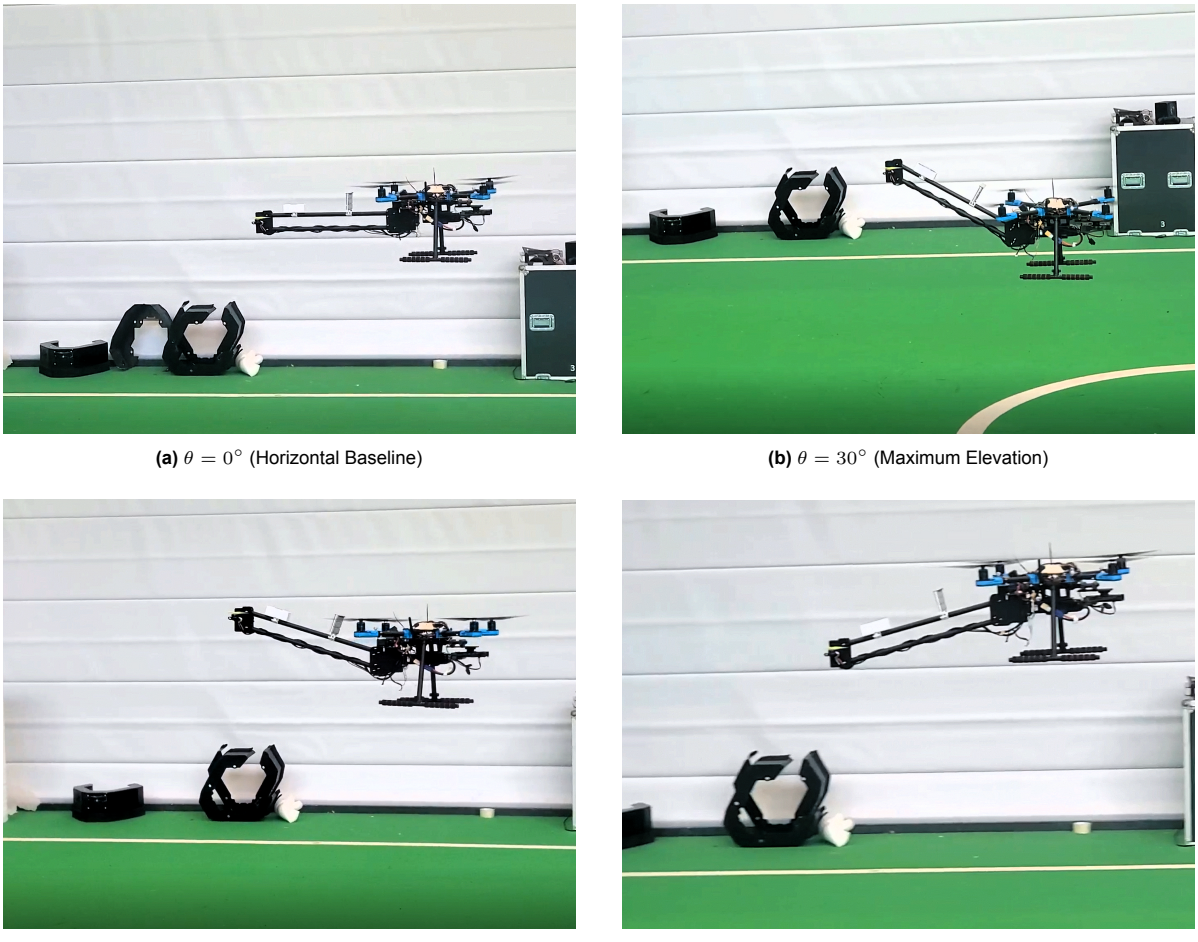
Substituting the software-assumed torque ($\tau_{y,soft}$) and defining the total main rotor lift as $T_{main} = T_{front} + T_{rear}$, the relationship between the commanded software torque and the physical reality simplifies to:

$$\tau_{y,phys} = \tau_{y,soft} - \Delta x_{cg} \cdot T_{main} \tag{7.5}$$

This formulation explains the re-emergence of the steady-state tracking error. The term $\Delta x_{cg} \cdot T_{main}$ represents a continuous, unmodeled nose-down pitching moment that is proportional to the total lift generated by the main rotors. To maintain a stable hover ($\tau_{y,phys} = 0$), the flight controller must constantly output a positive pitch command ($\tau_{y,soft} > 0$).

Because the software's feed-forward model is unaware of the Δx_{cg} translation, a steady-state pitch tracking error emerges as the I-term compensates for the newly asymmetric moment arms. Hence, informing the model about the Δx_{cg} translation would lead to resolution. Dynamically updating the Control Allocator's geometric matrix, specifically shifting the main rotor longitudinal coordinates relative to the new CoG, would realign the software model with physical reality, generating asymmetric feed-forward thrust commands and directly eliminating the tracking offset.

7.3. Phase 3: Parametric Kinematic Evaluation



(a) $\theta = 0^\circ$ (Horizontal Baseline)

(b) $\theta = 30^\circ$ (Maximum Elevation)

(c) $\theta = 15^\circ$ (Elevated)

(d) $\theta = -15^\circ$ (Depressed)

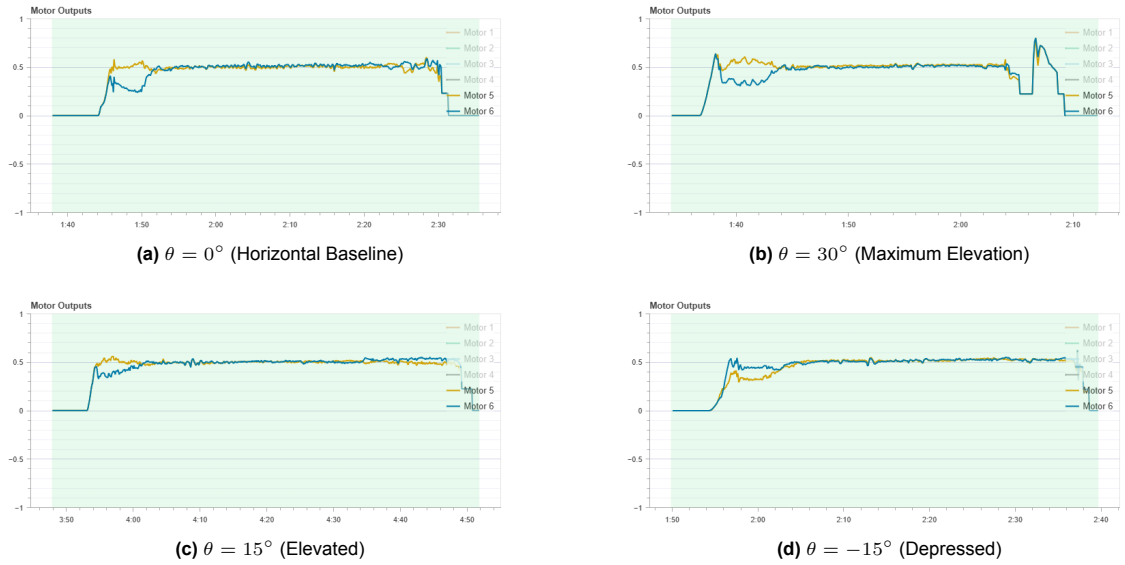
Figure 7.8: In-flight operation of the mechanism

With the actuator saturation risk resolved, the discrete parametric sweep was conducted using the redesigned PLA-CF brackets for root and tip links, locking the parallel linkage at $\theta = \{15°, -15°, 30°\}$ (seen in Figure 7.8). Because the AMC thrust requirement was theoretically established as a constant in Chapter 3, these tests were designed to evaluate the flight controller's ability to handle horizontal CoG translation, aerodynamic interference, and structural stress.

7.3.1. Theoretical Validation: The $\cos\theta$ Decoupling

A cross-examination of the Actuator Output (RCOUT) logs (plotted in Figure 7.9) across all tested angles produced the absolute validation of the thesis. As detailed in Table 7.1 for the full 500 g payload configuration, the mean headroom margin ($H_m\%$) stabilized at **50.36%, 49.99%, 50.08%, and 51.07%** for tests FT-10 ($0°$), FT-13 ($15°$), FT-16 ($-15°$), and FT-19 ($30°$), respectively.

This minimal variance of approximately $\pm 0.5\%$ explicitly proves that the tip-actuator effort required to maintain the Active Moment is mathematically decoupled from the pitch angle θ. This confirms the kinematic parallel-linkage hypothesis: because the tip link always remains perfectly horizontal, the vertical thrust completely cancels the active gravity moment regardless of boom elevation.



(a) $\theta = 0°$ (Horizontal Baseline)

(b) $\theta = 30°$ (Maximum Elevation)

(c) $\theta = 15°$ (Elevated)

(d) $\theta = -15°$ (Depressed)

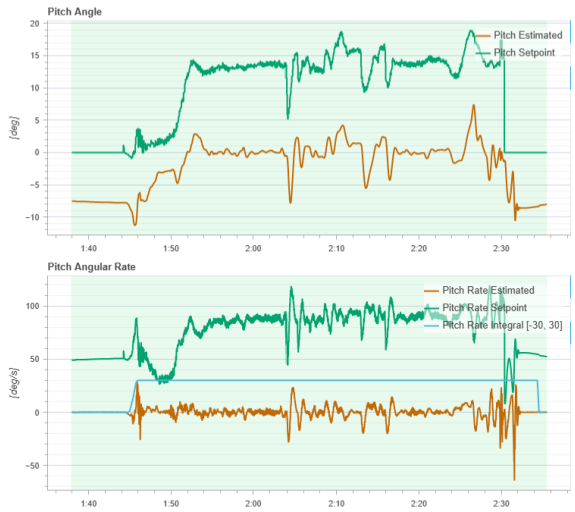
Figure 7.9: Motor Outputs across the discrete parametric sweep. Note the consistent baseline effort of approximately 50% throttle for Motors 5 and 6 across all kinematic states.

7.3.2. Elevated State Evaluation ($\theta = 15°$)

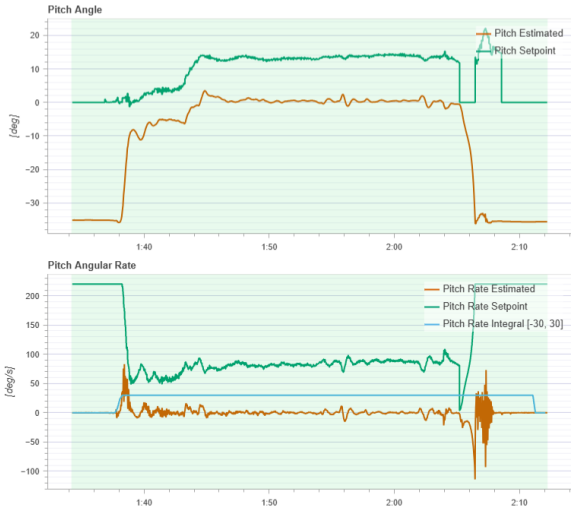
Flight tests conducted with the mechanism locked at $15°$ (FT-11,12,13) revealed an improved attitude control relative to the $0°$ baseline. Reviewing the 500 g Pitch Angular Tracking logs and plots (Figure 7.10), the steady-state error between the Pitch Estimated and Pitch Setpoint dropped.

The empirical data at this elevated state directly corroborate the CoG translation anomaly, as defined mathematically in subsection 7.2.2. At $0°$, the 500 g payload exerts its maximum horizontal lever arm, maximizing Δx_{cg}. However, as the boom pitches to $15°$, the horizontal projection is geometrically reduced to $L\cos(15°) \approx 483$mm. This 17 mm reduction in horizontal leverage directly decreases the asymmetric torque burden ($\Delta x_{cg} \cdot T_{main}$) placed on the primary quadrotor motors.

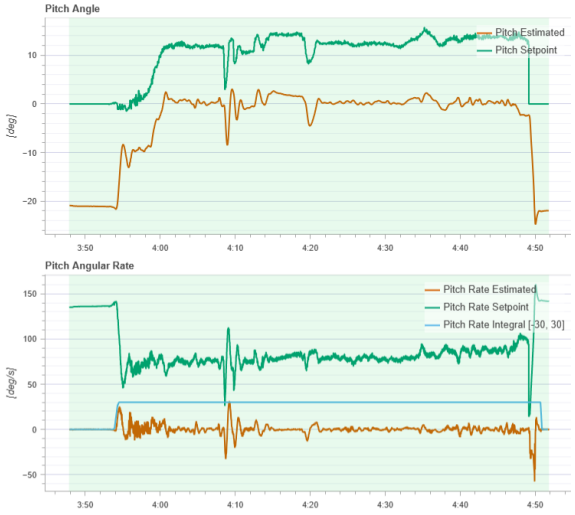
Additionally, the Vibration Metrics (Figure 7.11c) showed slight stabilization compared to $0°$, as the tip rotors began to elevate out of the immediate aerodynamic wake of the main chassis. In an Acceleration Power Spectral Density (PSD) plot, bright, solid horizontal lines represent the blade passage frequency (motor RPM $\times$ number of blades) and its harmonics. The more yellow an area is, the higher the frequency response at that time and frequency [28]. At $15°$, the high-frequency bands show slight broadening compared to $0°$, but they remain cohesive. The control allocation matrix manages the center-of-gravity shift without severely dividing motor effort.



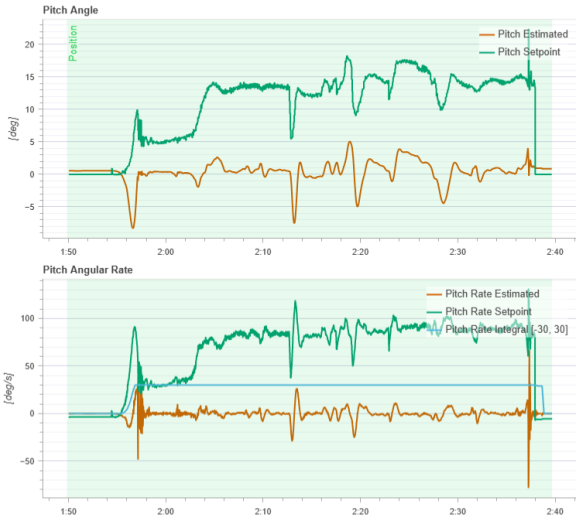
(a) $\theta = 0^\circ$ (Horizontal Baseline)



(b) $\theta = 30^\circ$ (Maximum Elevation)

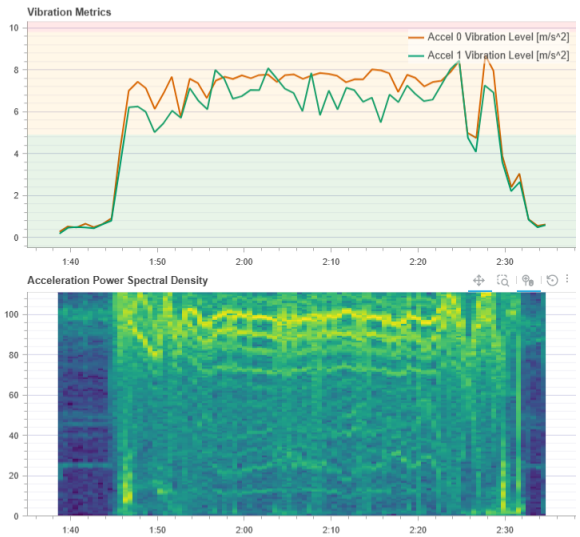


(c) $\theta = 15^\circ$ (Elevated)

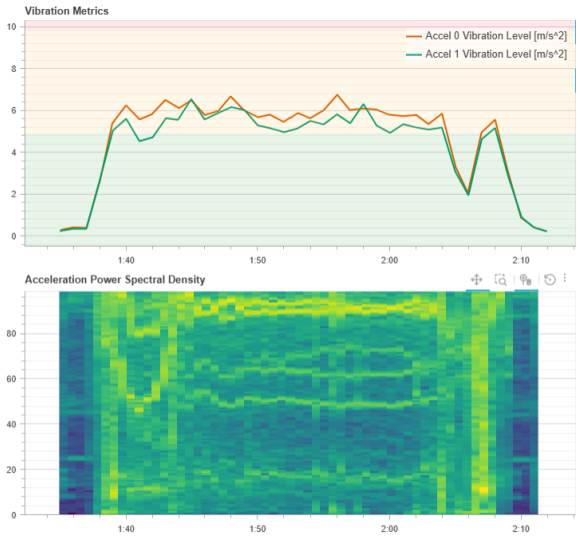


(d) $\theta = -15^\circ$ (Depressed)

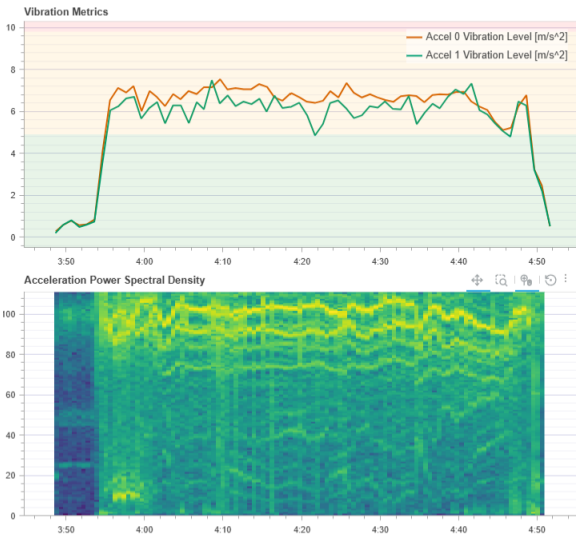
Figure 7.10: Plots of Pitch Angle and Angular rates at parametric θ angles under full load



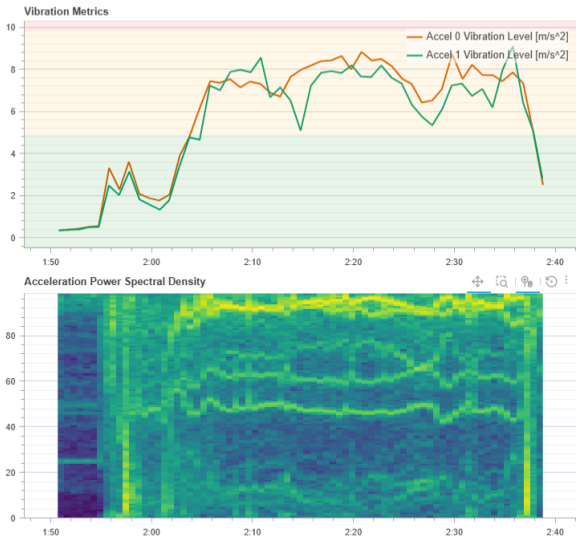
(a) $\theta = 0^\circ$ (Horizontal Baseline)



(b) $\theta = 30^\circ$ (Maximum Elevation)



(c) $\theta = 15^\circ$ (Elevated)



(d) $\theta = -15^\circ$ (Depressed)

Figure 7.11: Plots of Vibration Metrics and Spectral Density at parametric θ angles under full load

7.3.3. Depressed State Evaluation ($\theta = -15°$)

To validate the system's response to symmetrical horizontal loading but asymmetrical vertical loading, the mechanism was inverted to $-15°$ (FT-14,15,16). Mathematically, the horizontal CoG shift is identical to the elevated state ($L\cos(-15°) = L\cos(15°)$). The pitch tracking logs exhibited the same high-precision tracking and reduced steady-state error observed in the $+15°$ test.

While the kinematics are mathematically symmetric to the $+15°$ state, the dynamics are different. At $-15°$, the tip actuators are physically lower than the main chassis. Reviewing the Vibration Metrics (Figure 7.11d) for the $-15°$ reveal that the Accel 0 and Accel 1 vibration levels are relatively higher than the $+15°$ state, but still operating within the safe 6 to 10 m/s^2 range.

The PSD plot in this case shows the sudden emergence of prominent, oscillatory mid- to low-frequency bands. This signature indicates structural resonance specific to the depressed mechanism angle. This low-frequency noise forces the flight controller to counteract mechanical vibrations actively. This effect was evident during FT-16, where the flight controller required noticeably longer settling time for a stable hover.

7.3.4. Maximum Elevation State Evaluation ($\theta = 30°$)

The $30°$ locked state represented the maximum theoretical shift for the physical tests. The horizontal projection is minimized to $L\cos(30°) \approx 433$mm. This substantial 67 mm reduction centralizes the drone's mass, allowing the primary PID loops to operate at maximum symmetric efficiency. When evaluating the 250 g payload data (FT-18), Pitch RMSE reached its lowest loaded value across the entire sweep at just $3.03°$.

Most critically, the $30°$ elevation provides absolute aerodynamic free-stream isolation. Because the $30°$ angle elevates the tip-rotors and the transverse crossbar exactly 250 mm ($L\sin(30°)$) above the main drone chassis, they are completely extracted from the turbulent horizontal wake of the primary quadrotor blades. Reviewing the Vibration Metrics (Figure 7.11b), the vibration levels visibly drop, peaking at only 5-6 m/s^2 with a noticeably cleaner acceleration PSD, confirming increased aerodynamic efficiency.

7.4. Discussion and Implications for Dynamic Control

The discrete parametric sweep successfully mapped the absolute control boundaries of the active aerial manipulator. By isolating the mechanism at discrete kinematic states ($0°, \pm 15°, 30°$), the experimental dataset (Table 7.1) proves that the 1505 motor upgrade provides uniform, uninterrupted dynamic headroom across the required operational envelope.

The dataset provides empirical proof of the $\cos\theta$ kinematic decoupling theory derived in Chapter 3. As established in subsection 7.3.1, the minimal variance in $H_m\%$ ($\sim$50.5%) across all 500 g payload states validates the $\cos\theta$ kinematic decoupling theory. Because $H_m\%$ never drops below 48.5%, the control allocator retains ample thrust authority to correct dynamic disturbances without risking the actuator saturation that doomed the FT-04 baseline test.

Analyzing the closed-loop tracking errors also revealed a distinct decoupling in the system's management of induced strain. As the distal payload increases, the resulting static torque manifests almost entirely in the longitudinal axis. Despite the steady-state error, there was no observed loss of stability in flight performance across the path. In the baseline horizontal state ($0°$), increasing the payload from 0 g (FT-06) to 500 g (FT-10) degrades the Pitch RMSE from $0.885°$ to $13.119°$, with pitch rate errors scaling accordingly. While the introduction of the distal payload induced these steady-state pitch-tracking errors, analysis confirmed that the errors are due to a geometric mismatch. This anomaly can be directly resolved in software by realigning the Control Allocator's static geometry matrix parameters with the physical CoG translation (Δx_{cg}). Furthermore, the system structurally isolates this stress: Roll RMSE remains exceptionally tight, fluctuating only marginally between $0.56°$ and $1.15°$ across all test conditions. This mathematically validates the torsional rigidity of the 16 mm carbon fiber boom and the synchronous signal delivery of the 4-in-1 ESC, ensuring that longitudinal mass asymmetry does not seep into lateral instability. Yaw RMSE exhibits minor cross-axis coupling -rising from $1.93°$ to $5.34°$ under maximum load, but remains highly manageable, proving the counter-rotating tip-actuators effectively neutralize reactive torque.

During the -15° depressed state (FT-14,15,16), the distal mechanism is subjected to turbulent downwash from the primary base rotors. While the pilot observed that flight control felt marginally stiffer at this angle (FT-15), the telemetry reveals a Pitch RMSE of just 2.71° for the 250 g load. This indicates that the AMC architecture effectively suppresses these aerodynamic wake disturbances, keeping structural vibrations within the Pixhawk 6C IMU's safe operational margins. The designed PLA-CF joints exhibited good rigidity under these challenging conditions, effectively resisting delamination and resonance amplification.

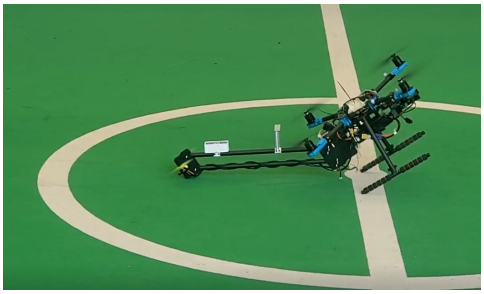


Figure 7.12: Pre-flight static resting posture at $\theta = 30^\circ$ due to CoG displacement.

An important physical constraint observed during testing is the pre-flight static resting posture. Under maximum payload, the severe forward-shifted CoG forces the drone to rest with the distal tip link grounded, except during the -15° state. Despite this extreme initial asymmetry at liftoff- most pronounced at $\theta = 30^\circ$ (Figure 7.12) and reflected in the initial transient spikes of the pitch plots -the controller achieves stable flight. This transient recovery demonstrates the system's robustness in rejecting ground-effect and unmodeled disturbances.

Having empirically proven that the static thrust requirement remains mathematically decoupled from the boom angle and that the airframe can autonomously reject the induced geometric torque offsets, the physical and software architectures are fully validated. These locked baseline tests successfully clear the architecture for the final phase of development: unlocking the mechanical joints, integrating real-time θ telemetry via absolute magnetic encoders, and closing the loop for fully dynamic, variable-pitch manipulation.

Table 7.1: Refined Test Log and Results with RMSE Data and $H_m\%$

ID	Payload	Hardware	S/W Config	Objective	Parameters	P_RMSE	PR_RMSE	Y_RMSE	YR_RMSE	R_RMSE	RR_RMSE	H_m%	Critical Insight
State (θ) = 0° (Horizontal)													
FT-01	Unloaded	1404 3850KV	Open-Loop	Validate mechanism operation	Default	0.556	3.822	0.818	2.626	0.493	3.533	–	Stable flight
FT-02	440 g	1404 3850KV	Open-Loop	Baseline Static Moment Comp.	Default	0.992	8.085	4.05	12.599	0.923	6.992	–	Stable flight. Tip rotor throttle close to 85%
FT-03	Unloaded	1404 3850KV	Closed-Loop	Validate mechanism operation	Default	7.767	50.573	1.38	4.685	0.647	4.095	67.101	Stable Flight. Offset observed in Pitch graphs
FT-04	440 g	1404 3850KV	Closed-Loop	Test mechanism working	Default	4.455	29.351	5.75	16.702	0.671	5.862	74.285	Takeoff failed
FT-05	Unloaded	1505 3750KV	Closed-Loop	Validate the upgraded motors	Default	20.859	134.564	7.264	19.684	1.254	3.769	60.674	Takeoff with uneven thrust
FT-06	Unloaded	1505 3750KV	Closed-Loop	Verify thrust allocation	CA_CT_4/5=3	0.885	5.337	1.934	5.311	0.563	3.267	67.694	Better flight stability
FT-07	250 g	1505 3750KV	Closed-Loop	Check flight operation	CA_CT_4/5=3	3.34	21.619	2.659	9.484	0.692	3.875	60.755	Stable flight
FT-08	500 g	1505 3750KV	Closed-Loop	Check flight operation at full payload	CA_CT_4/5=3	12.864	83.097	3.506	10.935	0.596	4.907	52.399	Less stable at takeoff
FT-09	500 g	1505 3750KV	Closed-Loop	Quick takeoff attempt	CA_CT_4/5=3, _HOVER=0.6	14.507	93.413	5.419	15.885	1.156	4.309	48.506	Unstable liftoff, but stability overtime
FT-10	500 g	1505 3750KV	Closed-Loop	Slower takeoff attempt	CA_CT_4/5=3, _HOVER=0.6	13.119	85.015	5.347	16.055	1.032	4.669	50.365	Stable liftoff and flight control
State (θ) = 15° (Elevated)													
FT-11	Unloaded	1505 3750KV	Closed-Loop	Check flight operation	CA_CT_4/5=3, _HOVER=0.6	0.652	4.101	0.941	6.65	0.76	3.322	67.481	Stable flight
FT-12	250 g	1505 3750KV	Closed-Loop	Check flight operation	CA_CT_4/5=3, _HOVER=0.6	3.253	20.708	3.207	11.117	1.02	6.25	59.716	Stable flight
FT-13	500 g	1505 3750KV	Closed-Loop	Check flight operation	CA_CT_4/5=3, _HOVER=0.6	12.295	79.626	2.61	7.524	0.711	4.839	49.997	Stable flight
State (θ) = -15° (Depressed)													
FT-14	Unloaded	1505 3750KV	Closed-Loop	Check flight operation	CA_CT_4/5=3, _HOVER=0.6	0.649	4.667	1.102	8.948	0.909	3.432	69.078	Stable Flight
FT-15	250 g	1505 3750KV	Closed-Loop	Check flight operation	CA_CT_4/5=3, _HOVER=0.6	2.717	17.563	1.784	6.247	0.709	3.888	60.268	Flight Control harder, but overall stable
FT-16	500 g	1505 3750KV	Closed-Loop	Check flight operation	CA_CT_4/5=3, _HOVER=0.6	12.356	80.013	2.84	7.903	0.674	6.633	50.084	Marginally stable flight
State (θ) = 30° (Extreme Elevation)													

Continued on next page...

Table 7.1: Refined Test Log and Results (Continued)

ID	Payload	Hardware	S/W Config	Objective	Parameters	P_RMSE	PR_RMSE	Y_RMSE	YR_RMSE	R_RMSE	RR_RMSE	H_m%	Critical Insight
FT-17	Unloaded	1505 3750KV	Closed-Loop	Check flight operation	CA_CT_4/5=3, _HOVER=0.6	0.795	4.922	0.969	4.537	0.663	3.592	67.885	Stable flight
FT-18	250 g	1505 3750KV	Closed-Loop	Check flight operation	CA_CT_4/5=3, _HOVER=0.6	3.032	19.362	3.759	12.106	1.003	4.615	60.181	Stable flight
FT-19	500 g	1505 3750KV	Closed-Loop	Check flight operation	CA_CT_4/5=3, _HOVER=0.6	14.02	88.014	5.706	16.022	0.898	5.868	51.074	Stable flight takeoff

8

Conclusion

This thesis conceptualized, modeled, and validated a novel active-thrust parallel manipulator designed to solve the payload-reach limitations inherent to non-contact aerial inspection. By rejecting traditional passive mass balancing in favor of distributed thrust compensation, the project demonstrated a highly scalable architecture that maintains UAV flight stability during severe Center of Gravity (CoG) shifts. Based on the work, the research questions can be answered as follows:

- **Kinematic Decoupling Proof:** The mathematical derivation proves that a parallel-link geometry ensures the active thrust vector remains perfectly vertical, thereby rendering the required Active Moment Compensation (AMC) thrust a kinematic constant independent of the manipulator's pitch angle. This proof led to simplified flight control, with the tip motors requiring $\sim 50\%$ thrust across all the pitch angles.
- **Advanced Structural Prototyping:** This research fabricated a lightweight, modular, and rigid 1:10 scaled carbon-fiber prototype, using PLA-CF brackets and optimized composite fastener ratios to mitigate localized stress concentrations against torsional forces induced by the tip rotors and other factors on the mechanism.
- **Digital Twin Integration:** A rigorously calibrated PX4-ROS2 and Gazebo SITL environment were developed. The PX4 Control Allocator was extended to a 6-motor geometry, and the tip-motor allocation and dual-mode routing architecture were successfully tested in simulation prior to physical deployment. The developed Simulation-to-Real workflow serves as a base for custom PX4-based drone mechanisms in general.
- **Real-World Experimental Validation:** The tests successfully isolated the variables of static torque, structural tension, and aerodynamic cross-axis coupling from the noise of closed-loop sensor dynamics. Experiments yielded insights into data trends, the flight controller's limits, and corrective measures. The aerial manipulator achieved the primary goal of stable flight across the structured physical flight-test matrix ($\theta = 0^\circ, \pm 15^\circ, 30^\circ$)

This research bridges the gap between theoretical kinematics concepts and real-world control implementation. By proving that the required thrust compensation can be achieved as a constant, independent of manipulator angle, this thesis eliminates the need for complex control modes to manage the static torque. The successful mitigation of unmodeled geometric offsets across challenging tests, combined with structural validation of the components, demonstrates the viability of the Active Moment Compensation (AMC) concept.

Beyond the scope of the scaled X500 prototype, the findings presented hold implications for the broader field of aerial robotics. The ability to manage an extended payload without affecting the base drone's stabilization limits effectively resolves the "Long-reach Weight Paradox." This method provides a pathway to deploying aerial manipulators for industrial NDT without requiring a massive drone chassis.

Future Outlook

While this thesis successfully validated the static kinematic and structural foundation of the active compensation architecture, critical steps remain to transition the system to a deployable industrial application. The current control stack needs further optimization to handle unmodelled load and CoG shifts effectively. The next task is to develop a dynamic geometric matrix update and identify additional PX4 parameters for better stability.

The subsequent phase of research would focus on unlocking the physical root joint and integrating an AS5048A absolute magnetic encoder directly into the flight stack. Using the baseline PID data from the locked parametric tests, a dynamic control loop could be implemented to stabilize the mechanism at discrete angles.

Furthermore, to deploy actual NDT payloads, such as penetrative X-ray tubes, the 1:10-scale prototype must be scaled to the target 2.5m heavy-lift platform. As the physical scale of the carbon fiber linkage increases, the boom's structural elasticity will inherently amplify the high-frequency vibrations induced by the tip rotors. To prevent critical sensor blurring during non-contact imaging, future iterations should explore integrating piezoelectric (PZT) sensors with localized active vibration-damping algorithms distributed along the manipulator links.

Ultimately, the theoretical models and empirically validated baseline architecture established in this thesis serve as a blueprint for a new class of dexterous, heavy-lift aerial manipulators capable of safely performing critical industrial interactions.

References

[1] Richard Abbott. *12.2.4. Mechanical Joints in Composite Panels*. Abbott Aerospace UK Ltd. 2019. URL: https://www.abbottaerospace.com/aa-sb-001/12-joints/12-2-mechanically-fastened-joints/12-2-4-mechanical-joints-in-composite-panels/.

[2] Ibrahim Abuzayed et al. "Design of Lightweight Aerial Manipulator with a CoG Compensation Mechanism". In: *2020 Advances in Science and Engineering Technology International Conferences (ASET)*. Feb. 2020, pp. 1–5. DOI: 10.1109/ASET48392.2020.9118288. URL: https://ieeexplore.ieee.org/document/9118288.

[3] Ayham AlAkhras et al. "The Design of a Lightweight Cable Aerial Manipulator with a CoG Compensation Mechanism for Construction Inspection Purposes". en. In: *Applied Sciences* 12.3 (Jan. 2022), p. 1173. ISSN: 2076-3417. DOI: 10.3390/app12031173. URL: https://www.mdpi.com/2076-3417/12/3/1173.

[4] G. K. Ananda et al. "Design Methodology for a Dynamically-Scaled General Aviation Aircraft". In: *AIAA Aviation Forum*. 2017. URL: https://m-selig.ae.illinois.edu/pubs/AnandaVahoraDantskerSelig-2017-AIAA-Paper-2017-4077-DesMethodforDynScalingGA.pdf.

[5] Autodesk. *Autodesk Fusion*. Version 2703.1.20 x86_64. Computer-aided design (CAD), computer-aided manufacturing (CAM), and computer-aided engineering (CAE) software. 2026. URL: https://www.autodesk.com/products/fusion-360.

[6] Avular. *Shocking Precision – Case Studies*. 2026. URL: https://www.avular.com/case-studies/Shocking-Precision.

[7] K. Baizid et al. "Behavioral control of unmanned aerial vehicle manipulator systems". en. In: *Autonomous Robots* 41.5 (June 2017), pp. 1203–1220. ISSN: 1573-7527. DOI: 10.1007/s10514-016-9590-0. URL: https://doi.org/10.1007/s10514-016-9590-0 (visited on 02/10/2026).

[8] Mengyi Bi et al. "Advances, challenges, and future directions of UAV/drone-based active nondestructive testing". In: *Nondestructive Testing and Evaluation* 0.0 (Jan. 2026), pp. 1–42. ISSN: 1058-9759. DOI: 10.1080/10589759.2025.2601323. URL: https://doi.org/10.1080/10589759.2025.2601323.

[9] Annemiek G.C van Boeijen, J.J. Daalhuizen, and Jelle Zijlstra. *Delft Design Guide: Perspectives, models, approaches, methods*. English. 2nd. BIS Publishers, 2020. ISBN: 978-90-6369-540-8.

[10] Hossein Bonyan Khamseh, Farrokh Janabi-Sharifi, and Abdelkader Abdessameud. "Aerial manipulation-A literature survey". In: *Robotics and Autonomous Systems* 107 (Sept. 2018), pp. 221–235. ISSN: 0921-8890. DOI: 10.1016/j.robot.2018.06.012. URL: https://www.sciencedirect.com/science/article/pii/S0921889017305535.

[11] Mark Drela. *First-Order DC Electric Motor Model*. Technical Note. Cambridge, MA: Massachusetts Institute of Technology, 2007.

[12] Gen Endo et al. "A Proposal of Super Long Reach Articulated Manipulator with Gravity Compensation using Thrusters". In: *2018 IEEE/ASME International Conference on Advanced Intelligent Mechatronics (AIM)*. July 2018, pp. 1414–1419. DOI: 10.1109/AIM.2018.8452705. URL: https://ieeexplore.ieee.org/document/8452705.

[13] Felix Huber et al. "First analysis and experiments in aerial manipulation using fully actuated redundant robot arm". In: *2013 IEEE/RSJ International Conference on Intelligent Robots and Systems*. Nov. 2013, pp. 3452–3457. DOI: 10.1109/IROS.2013.6696848. URL: https://ieeexplore.ieee.org/abstract/document/6696848.

[14] A.E. Jimenez-Cano et al. "Control of an aerial robot with multi-link arm for assembly tasks". In: *2013 IEEE International Conference on Robotics and Automation*. May 2013, pp. 4916–4921. DOI: 10.1109/ICRA.2013.6631279. URL: https://ieeexplore.ieee.org/abstract/document/6631279.

[15] Somasundar Kannan, Miguel A. Olivares-Mendez, and Holger Voos. “Modeling and Control of Aerial Manipulation Vehicle with Visual sensor*”. In: *IFAC Proceedings Volumes*. 2nd IFAC Workshop on Research, Education and Development of Unmanned Aerial Systems 46.30 (Jan. 2013), pp. 303–309. ISSN: 1474-6670. DOI: 10.3182/20131120-3-FR-4045.00053. URL: https://www.sciencedirect.com/science/article/pii/S1474667015403106.

[16] Hyunyong Lee et al. “A drone-driven X-ray image-based diagnosis of wind turbine blades for reliable operation of wind turbine”. In: *IEEE Access* 12 (2024), pp. 56141–56158.

[17] Steven Macenski et al. “Robot Operating System 2: Design, architecture, and uses in the wild”. In: *Science Robotics* 7.66 (2022), eabm6074. DOI: 10.1126/scirobotics.abm6074.

[18] Mohammad Malakouti Khah, Sayyed Majid Esmailifar, and Sepehr Saadat. “Design and development of a novel multirotor configuration with counter-rotating coaxial propellers”. In: *Scientific Reports* 14.1 (2024), p. 11580.

[19] Michele Marolla, Jonathan Cacace, and Vincenzo Lippiello. “Design and Control of a Novel High Payload Light Arm for Heavy Aerial Manipulation Tasks:” en. In: *Proceedings of the 20th International Conference on Informatics in Control, Automation and Robotics*. Rome, Italy: SCITEPRESS - Science and Technology Publications, 2023, pp. 465–473. ISBN: 978-989-758-670-5. DOI: 10.5220/0012202900003543. URL: https://www.scitepress.org/DigitalLibrary/Link.aspx?doi=10.5220/0012202900003543.

[20] Bas Meere et al. “X-ray Image Generation for Robotic Radiography: a Case Study on Motion Blur in Drone-Based Wind Turbine Inspections”. In: *Journal of Nondestructive Evaluation* 44.4 (Dec. 2025). ISSN: 0195-9298. DOI: 10.1007/s10921-025-01279-6. URL: https://www.scopus.com/pages/publications/105018111402.

[21] Lorenz Meier and The PX4 Contributors. *PX4 Autopilot*. 2016. DOI: 10.5281/zenodo.595432. URL: https://px4.io.

[22] Arthur P. Mendez, James F. Whidborne, and Lejun Chen. “Wind Preview-Based Model Predictive Control of Multi-Rotor UAVs Using LiDAR”. In: *Sensors* 23.7 (2023). ISSN: 1424-8220. DOI: 10.3390/s23073711. URL: https://www.mdpi.com/1424-8220/23/7/3711.

[23] Gerardo Julián Pérez Mendoza et al. “Mechanical Properties of PLA with CF Printed at 40%, 80% and 100% Infill Percentages”. In: *Microscopy and Microanalysis* 29.Supplement$_1$ (Aug. 2023), pp. 1447–1449. ISSN: 1431-9276. DOI: 10.1093/micmic/ozad067.744. eprint: https://academic.oup.com/mam/article-pdf/29/Supplement_1/1447/50933956/ozad067.744.pdf. URL: https://doi.org/10.1093/micmic/ozad067.744.

[24] Xiangdong Meng, Yuqing He, and Jianda Han. “Survey on Aerial Manipulator: System, Modeling, and Control”. en. In: *Robotica* 38.7 (July 2020), pp. 1288–1317. ISSN: 0263-5747, 1469-8668. DOI: 10.1017/S0263574719001450. URL: https://www.cambridge.org/core/journals/robotica/article/survey-on-aerial-manipulator-system-modeling-and-control/5FDD2404D65EF73477CF10CA62B69720.

[25] Abeje Y. Mersha, Stefano Stramigioli, and Raffaella Carloni. “Exploiting the dynamics of a robotic manipulator for control of UAVs”. In: *2014 IEEE International Conference on Robotics and Automation (ICRA)*. May 2014, pp. 1741–1746. DOI: 10.1109/ICRA.2014.6907086. URL: https://ieeexplore-ieee-org.tudelft.idm.oclc.org/document/6907086 (visited on 01/13/2026).

[26] Yoshinori Ohnishi et al. “Development of a 4-joint 3-DOF robotic arm with anti-reaction force mechanism for a multicopter”. In: *2017 IEEE/RSJ International Conference on Intelligent Robots and Systems (IROS)*. Sept. 2017, pp. 985–991. DOI: 10.1109/IROS.2017.8202265. URL: https://ieeexplore.ieee.org/abstract/document/8202265 (visited on 02/10/2026).

[27] Siyi Pan and Gen Endo. “Flying watch: an attachable strength enhancement device for long-reach robotic arms”. en. In: *ROBOMECH Journal* 6.1 (May 2019), p. 5. ISSN: 2197-4225. DOI: 10.1186/s40648-019-0133-2. URL: https://doi.org/10.1186/s40648-019-0133-2.

[28] PX4 Autopilot Contributors. *Flight Review: Vibration*. 2026. URL: https://docs.px4.io/main/en/log/flight_review#vibration.

[29] PX4 Development Team. *Control Allocation (Mixing)*. PX4 Autopilot. 2025. URL: https://docs.px4.io/main/en/concept/control_allocation#control-allocation-mixing.

[30] PX4 Development Team. *Controller Diagrams*. PX4 Autopilot. 2025. URL: https://docs.px4.io/main/en/flight_stack/controller_diagrams.

[31] Stimulus Programmamanagement. *Shocking Precision: X-Ray Tech and Autonomous Drones Power the Future of Grid Inspections*. 2026. URL: https://www.stimulus.nl/opzuid-2021-2027/avada_portfolio/shocking-precision-x-ray-tech-and-autonomous-drones-power-the-future-of-grid-inspections/.

[32] Alejandro Suarez et al. “Design of a lightweight dual arm system for aerial manipulation”. In: *Mechatronics* 50 (Apr. 2018), pp. 30–44. ISSN: 0957-4158. DOI: 10.1016/j.mechatronics.2018.01.005. URL: https://www.sciencedirect.com/science/article/pii/S0957415818300011.

[33] Miguel Ángel Trujillo et al. “Novel Aerial Manipulator for Accurate and Robust Industrial NDT Contact Inspection: A New Tool for the Oil and Gas Inspection Industry”. en. In: *Sensors* 19.6 (Mar. 2019). ISSN: 1424-8220. DOI: 10.3390/s19061305. URL: https://www.mdpi.com/1424-8220/19/6/1305 (visited on 02/19/2026).

[34] Yusuke Ueno et al. “Development of Hiryu-II: A Long-Reach Articulated Modular Manipulator Driven by Thrusters”. In: *IEEE Robotics and Automation Letters* 5.3 (July 2020), pp. 4963–4969. ISSN: 2377-3766. DOI: 10.1109/LRA.2020.3004775. URL: https://ieeexplore.ieee.org/document/9126164.

[35] Hyunsoo Yang et al. “LASDRA: Large-Size Aerial Skeleton System with Distributed Rotor Actuation”. In: *2018 IEEE International Conference on Robotics and Automation (ICRA)*. May 2018, pp. 7017–7023. DOI: 10.1109/ICRA.2018.8460713. URL: https://ieeexplore.ieee.org/document/8460713.

[36] Yehui Zhang, Zhaoying Wang, and Wei Dong. “An Aerial Non-contact Detection System For Quayside Crane Using A Hexacopter”. In: *2023 IEEE International Conference on Real-time Computing and Robotics (RCAR)*. July 2023, pp. 774–779. DOI: 10.1109/RCAR58764.2023.10249376. URL: https://ieeexplore.ieee.org/abstract/document/10249376.

[37] Moju Zhao et al. “Design, Modeling, and Control of an Aerial Robot DRAGON: A Dual-Rotor-Embedded Multilink Robot With the Ability of Multi-Degree-of-Freedom Aerial Transformation”. In: *IEEE Robotics and Automation Letters* 3.2 (Apr. 2018), pp. 1176–1183. ISSN: 2377-3766. DOI: 10.1109/LRA.2018.2793344. URL: https://ieeexplore.ieee.org/document/8258850/authors (visited on 12/24/2025).

A

SITL Software Configuration Architecture

This appendix details the specific software architecture, configuration parameters, and execution pipeline utilized to construct the Software-in-the-Loop (SITL) digital twin discussed in Chapter 6. While the primary manuscript focuses on the theoretical derivation of the active compensation kinematics and the mathematical extension of the Control Allocator, this section provides the technical details of the framework necessary for system reproducibility.

A.1. ROS 2 Workspace and Package Structure

The custom ROS 2 workspace (`drone_gimbal_simulation`) contains three primary packages:

1. **`drone_gimbal_gz`** – Gazebo model definitions (URDF/XACRO), launch files, configuration YAML files, and the `launch_utils.py` orchestration module.
2. **`gz_control_scripts`** – ROS 2 nodes for boom rotor control and telemetry.
3. **`control_drone_gimbal_msgs`** – Custom message definitions for the gimbal control interface.

A.2. PX4 Airframe Geometry and ESC Mapping

Custom Airframe: 4012_gz_x500_boom

A new airframe init script was created at the PX4 firmware path:
ROMFS/px4fmu_common/init.d-posix/airframes/4012_gz_x500_boom

This script extends the base multirotor geometry (`CA_AIRFRAME = 0`) from 4 to 6 rotors by declaring two additional rotors with the following geometry parameters:

Table A.1: Overview of the Geometric Parameters set in CA

Parameter	Rotor 4 (CCW)	Rotor 5 (CW)	Description
`CA_ROTOR_PX`	+0.678	+0.678	Forward offset from CG (m)
`CA_ROTOR_PY`	-0.12	+0.12	Lateral offset from CG (m)
`CA_ROTOR_PZ`	-0.105	-0.105	Vertical offset below CG (m)
`CA_ROTOR_KM`	+0.05	-0.05	Yaw moment coeff (sign = spin direction)
`CA_ROTOR_AZ`	-1.0	-1.0	Thrust axis (upward in NED) – default

The positive KM value indicates counter-clockwise rotation (viewed from above) and the negative value indicates clockwise rotation. The counter-rotating arrangement ensures that equal thrust from both boom rotors produces zero net yaw torque.

ESC-to-Gazebo Bridge Mapping

The PX4 Gazebo bridge (`GZMixingInterfaceESC`) publishes a single `gz.msgs.Actuators` message containing a velocity array with one slot per active ESC channel. The mapping is configured through `SIM_GZ_EC_FUNC` parameters

Table A.2: Overview of Function Mapping

ESC Chan	Output Function	Motor Index	Gazebo Slot	Physical actuator
1	101 (Motor 1)	0	velocity[0]	Main rotor 0
2	102 (Motor 2)	1	velocity[1]	Main rotor 1
3	103 (Motor 3)	2	velocity[2]	Main rotor 2
4	104 (Motor 4)	3	velocity[3]	Main rotor 3
5	105 (Motor 5)	4	velocity[4]	Boom rotor 0
6	106 (Motor 6)	5	velocity[5]	Boom rotor 1

Each Gazebo `MulticopterMotorModel` plugin instance subscribes to the same `command/motor_speed` topic and selects its command from the array using the configured `motorNumber` parameter. This contiguous indexing scheme is required by the `GZMixingInterfaceESC` implementation, which counts active outputs sequentially.

The ESC minimum values for the boom channels are set to 500 (compared to 150 for the main rotors), providing an idle spin speed when armed that reduces the spool-up latency for the Control Allocator.

A.3. Launch Configuration and Dual-Mode YAML

The simulation is orchestrated by a single ROS 2 launch file (`combi_drone_gimbal.launch.py`) that reads a YAML configuration file and executes the following sequence:

1. **Gazebo server and client** – Launched with the selected world file and headless/GUI configuration.
2. **Model spawning** – The composite XACRO model is processed with the appropriate arguments (gimbal model, boom enabled, PX4 mode) and spawned into the running Gazebo world.
3. **PX4 SITL process** – The PX4 binary is started with `PX4_SYS_AUTOSTART` set to the configured airframe ID and `PX4_GZ_MODEL_NAME` set to the spawned model name. PX4 waits for the Gazebo spawn to complete before initializing.
4. **ROS–Gazebo bridges** – `ros_gz_bridge` instances are created for odometry, joint states, and gimbal command topics. In Path A, an additional bridge is created for the boom rotor topic; in Path B, this bridge is suppressed to avoid conflicts with PX4's internal Gazebo bridge.
5. **Telemetry forwarding** – MAVProxy is started for telemetry forwarding to ground control stations.
6. **RViz** – An optional RViz instance is launched for real-time visualization of the robot model and TF tree.

The XACRO processing pipeline generates two robot descriptions from the same source file: one for Gazebo (using Gazebo-relative mesh paths) and one for RViz (using ROS package-relative mesh paths). This dual-description approach avoids path resolution conflicts between the Gazebo model system and the ROS resource locator. The full launch process is visualized in Figure 6.1.

Mode Selection

The mode is configured through the launch YAML file:

```
# Path B (recommended):
boom_enabled: true
boom_px4_mode: true
px4_autostart: '4012'

# Path A (bench testing):
boom_enabled: true
boom_px4_mode: false
```

```
# px4_autostart defaults to '4001'
```

The launch system passes `boom_px4_mode` as an XACRO argument, which conditionally selects the `commandSubTopic` and `motorNumber` values in the boom motor plugin definitions. The `px4_autostart` parameter overrides the PX4 `SYS_AUTOSTART` environment variable to select the appropriate airframe init script.

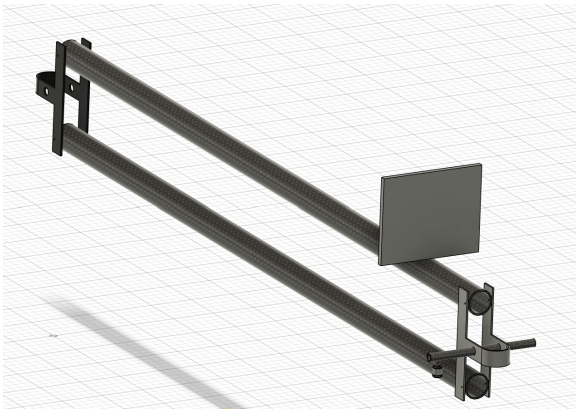
A.4. Verification

The geometric consistency was thoroughly verified, with systematic cross-check between the Gazebo model (`model.xacro`), the configuration of the PX4 airframe (`4012 _gz _x500 _boom`), and the schema of the parameters of the PX4 CA module (`module.yaml`). The verification confirmed:

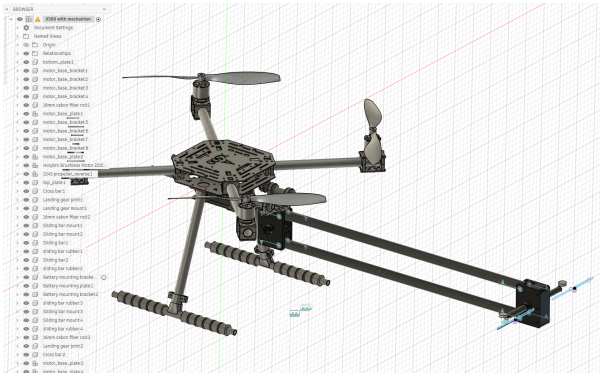
- All rotor positions (PX, PY, PZ) in the airframe match the corresponding XACRO properties to millimeter precision.
- The yaw moment coefficients (KM) correctly encode the counter-rotating arrangement (CCW = +0.05, CW = -0.05).
- The thrust axis defaults (AX = 0, AY = 0, AZ = -1) correctly specify upward-pointing thrust in the NED frame.
- The thrust coefficient (CT = 6.5, default) is identical for all six rotors, which is correct because the CA normalizes relative effectiveness - the physical thrust difference between main and boom rotors is handled by the specifically defined Gazebo motor constants.
- The ESC channel-to-motor-function mapping (101–106) is contiguous and within the valid range defined by `output_functions.yaml` (Motor start = 101, count = 12).
- The `GZMixingInterfaceESC` bridge correctly sizes the velocity array to the number of active ESC channels (6) and performs a 1:1 index mapping from the output buffer to the Actuators message.
- The Gazebo environment maintains an average Real-Time Factor (RTF) of 0.95 throughout these simulation runs, proving the validity of the SITL.

B

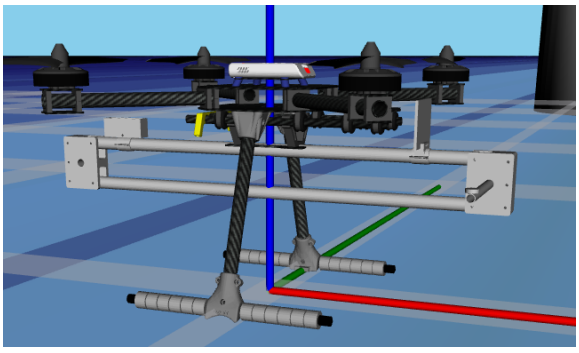
Pictures during the process



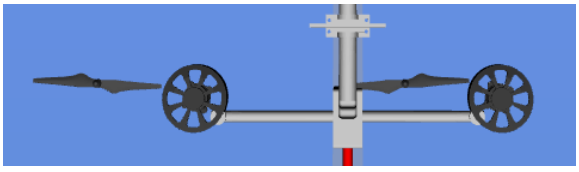
(a) Preliminary CAD render



(b) Final model attached



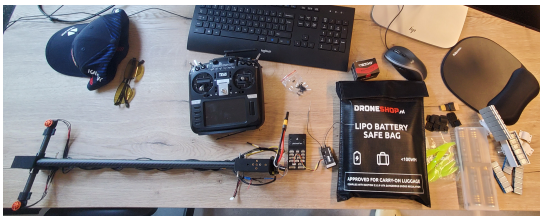
(c) Mechanism aligning in the RViz



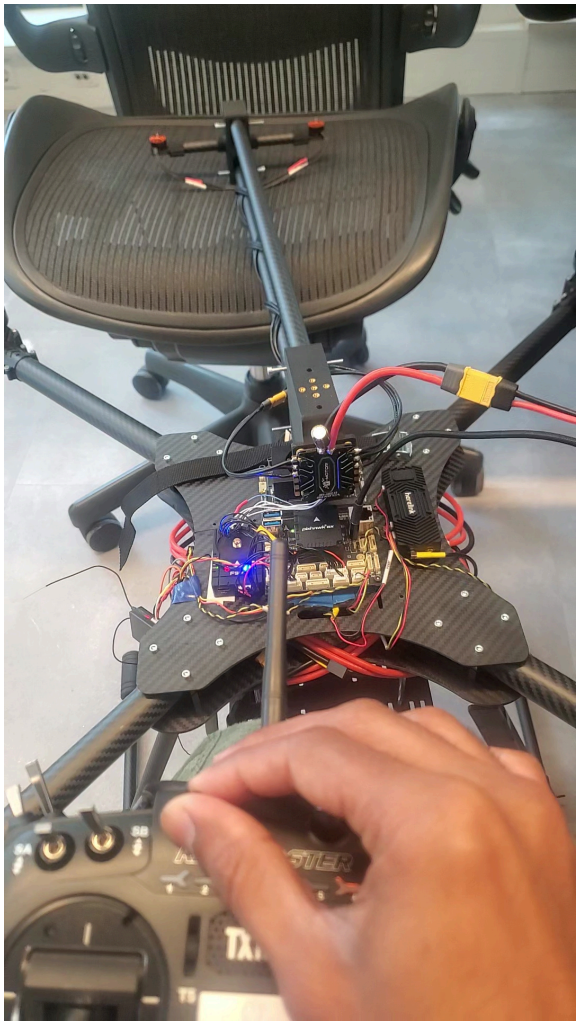
(d) Motors and propellers before alignment



(a) Weights strip



(b) Entire parts used for testing



(c) Testing the electronics

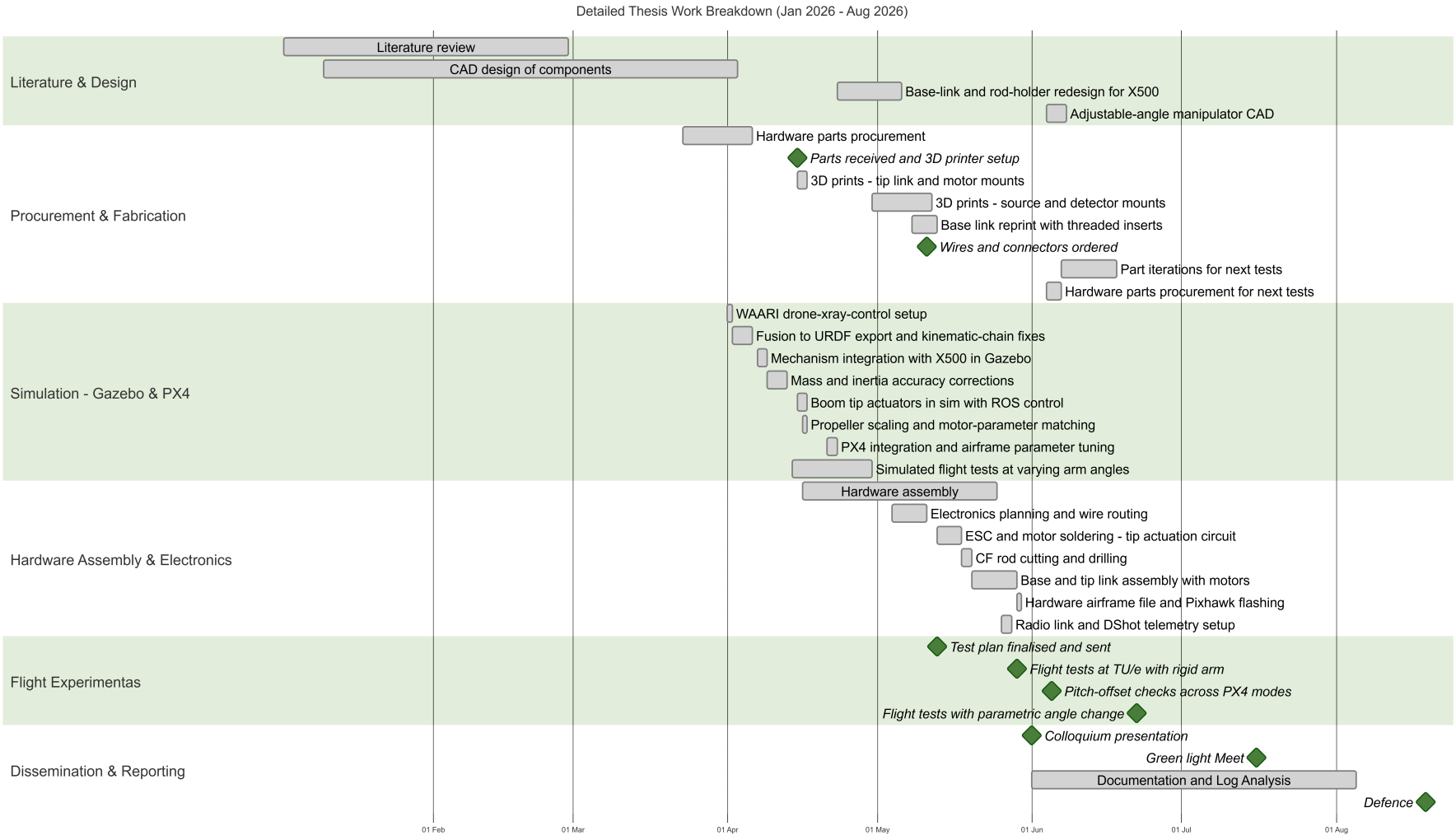


Figure B.3: Detailed Thesis Gantt Chart